Monthly Notices
of the
ROYAL ASTRONOMICAL SOCIETY

MNRAS **509,** 327–344 (2022)
Advance Access publication 2021 October 20

https://doi.org/10.1093/mnras/stab3005

Polycyclic aromatic hydrocarbons and the ionized gas in galaxies with active nuclei

A. Silva-Ribeiro [1]★ A. C. Krabbe [1]★ C. M. Canelo [2] A. F. Monteiro,[1] Dinalva A. Sales [3] J. A. Hernandez-Jimenez [1] and D. P. P. Andrade[4]

[1]*Instituto de Pesquisa e Desenvolvimento, Universidade do Vale do Paraíba, São José dos Campos 12244-000, Brazil*
[2]*Instituto de Astronomia, Geofísica e Ciências Atmosféricas, Departamento de Astronomia, Universidade de São Paulo, São Paulo 05508-090, Brazil*
[3]*Instituto de Matemática, Estatística e Física, Universidade Federal do Rio Grande, Rio Grande do Sul 96203-900 , Brazil*
[4]*Observatório do Valongo, Universidade Federal do Rio de Janeiro, Rio de Janeiro 20080-090, Brazil*

Accepted 2021 October 14. Received 2021 October 14; in original form 2021 July 26

ABSTRACT

We present a study for a sample of galaxies with active nuclei to characterize the main type of PAH molecules present in these objects and the local physical conditions of their irradiating sources, as well as the characteristics of the residing ionized gas, by combining optical and infrared data. Photoionization models were built with the CLOUDY code to reproduce optical emission line ratios in combination with PAH intensity ratios. We find that the species containing 10−82 carbon atoms are the most abundant in the sample. We suggest that family of species with only two or three fused rings of and a nitrogen hanging, such as small aromatic amides are important targets worthy of consideration in future experimental/theoretical as well as observational studies. We find that the AGN photoionization models reproduce most of the observational data in the log (6.2/11.3) versus log ([N II] λ6584/H α) diagram with the optical to X-ray spectral index of $\alpha_{ox} = -1.4$. The flux of small PAH, as well as the flux of ionized PAHs and PANH, decrease as the logarithm of the ionization parameter (log U) increases. The 6.2/11.3 PAH intensity ratio presents an anti correlation between the oxygen abundance and log U. Finally, we found that the ionization degree of PAH species increases with the decreasing of the 11.3/7.7 ratio and the log U, in agreement with the models proposed by Draine & Li.

Key words: astrochemistry – methods: data analysis – ISM: molecules – galaxies: active – galaxies: nuclei.

1 INTRODUCTION

Polycyclic Aromatic Hydrocarbons (PAHs) are organic compounds that contain two or more fused benzene rings and can also form large aromatic structures. Although the term PAHs refers to molecules containing only carbon and hydrogen atoms, the more general term 'polycyclic aromatic compounds' also includes the functional derivatives, just like nitro-PAHs, Oxy-PAHs, and the heterocyclic analogues. Studies show that PAHs represent one of the most abundant forms of carbon in the Universe, with approximately 15 per cent of the elemental carbon of the Universe is in the form of PAHs (Candian, Zhen & Tielens 2019). Besides, PAHs have an important role in heating the interstellar medium (ISM) since they have low ionization potential (Tielens 2008). This class of molecules is often observed in a wide range of astrophysical environments, including extragalactic sources such as Seyferts (Sys) and Starbursts (SBs) galaxies (Brandl et al. 2006; Smith et al. 2007; Sales, Pastoriza & Riffel 2010; Sales et al. 2013). They present stronger emission bands at 3.3, 6.2, 7.7, 8.6, 11.2, and 12.7 μm wavelength (e.g. Li 2020).

There is an astrobiological interest in PAHs due to their potential role in the formation of protocells, which may help to evaluate possible pathways for the origins of life on the early Earth. Like PAHs, Nitrogen-containing PAHs, known as PANHs, can fragment and form pre-biotic molecules, such as ethanol and amino acids (Ehrenfreund et al. 2006). In addition, such species can self-assemble, originating from the formation of protocells (Schrum, Zhu & Szostak 2010).

Canelo et al. (2018) analysed the 6.2-μm PAH emission band for 155 predominantly SB-dominated galaxies and distributed it into the Peeters' A, B, and C classes (Peeters et al. 2002), revealing a predominance of 67 per cent of Class A sources with band profiles corresponding to a central wavelength near 6.22 μm, which can only be explained by PANHs (Hudgins, Bauschlicher & Allamandola 2005). In this way, the PANHs, in addition to nitrogen in the gas phase and ices of the ISM, could be another reservoir of nitrogen in the Universe.

Studies have shown that the physical conditions of the object under study at radiation and metallicity levels, for example, affect both approaches. Hanine et al. (2020) found that the size of the formed PAH species increases roughly with increasing temperature up to 800 K, forming rings up to 32 carbon atoms and being correlated with the level of dehydrogenation, which can make these molecules highly reactive (Chen 2018), characteristic that can intensify the formation of large PAHs. Seok, Hirashita & Asano (2014), for example, concluded that the PAH abundance is low at low metallicities ($Z < 0.1\,Z_{\odot}$), but increases rapidly beyond a certain metallicity ($Z > 0.3\,Z_{\odot}$) by chemical evolution model in galaxies.

★ E-mail: adrianaufma@yahoo.com.br (AS-R); angela.krabbe@gmail.com (ACK)

On other hand, Maragkoudakis et al. (2018) found that variations on the 17-μm PAH band depend on the object type, however, there is no dependence on metallicity for both extragalactic H II regions and galaxies.

PAHs are also important molecules from the galactic diagnosis perspective because their emissions can be used as a calibrator for star formation in galaxies (e.g. Shipley et al. 2016; Maragkoudakis et al. 2018). Such peculiarity has been a motivating factor for studying the presence of PAHs in active galaxy nuclei (AGNs). Sy galaxies are a type of AGNs whose notoriety show presence of PAH emission lines. The ionization of PAH molecules, as well as ionized gas surrounding central engine of the Sy galaxies, is dominated by the hardness radiation coming from accreting disc of the supermassive black hole environment. Interestingly, Madden et al. (2006) and Maragkoudakis et al. (2018) have found that the total PAH/Very Small Grains (VSG) intensity ratio decreases with increasing radiation hardness, as traced by [Ne III]/[Ne II], indicating that harder radiation fields are largely responsible for the destruction of PAHs in low-metallicity regions. In addition, Sales et al. (2010, 2013) have studied 186 active and star-forming galaxies and could infer that active galaxies seems to present larger PAH molecules ($\geq$ 180 carbon atoms) than star-forming galaxies. They propose that PAH molecules can survive near to AGNs since their dusty tori is likely to provide column densities necessary to shield PAHs from the hard radiation field (see also Alonso-Herrero et al. 2014; Ruschel-Dutra et al. 2014).

The nuclear region of the Sy and SB are excellent objects for studying the signatures of PAHs in order to map the main species of PAHs that are contributing to the emissions in the IR of Sy and SB galaxies. Additionally, the presence of metallic emission lines, such as [O II] λ 3727, [O III] λ 4363, [O III] λ 4959, [O III] λ 5007, [N II] λ 5755, [N II] λ 6548, [N II] λ 6584, [S II] λ 6717, and [S II] λ 6731, which are present in Sy and SB galaxies make it possible to estimate the physical conditions (oxygen abundance, density, and electronic temperature) of the ionized gas regions. Besides, the ratio of emission lines in combination with photoionization models can be used to determine the hardness of ionizing source and the metallicity of the gas. In this context, it is the possible to verify correlations between the ionized gas regions and the photodissociation regions where PAHs persist.

Concerning the emission features at IR and optical wavelengths, studies have shown (e.g Schlemmer, Giesen & Mutschke 2014) that large carbon-based molecules (with $\sim$ 10–100 atoms) in the gas phase, such as PAHs, long carbon chains or fullerenes should be possible carriers of Diffuse Interstellar Bands (DIBs) and the Unidentified Infrared (UIR) bands. However, the identification of the carriers of DIBs remains to be examined, with the exception of five bands attributed to C_{60}^{+} Tielens (2013) and Campbell et al. (2015). In this sense, the analysis of potential emitting molecules of the PAH population in astrophysical sources in comparison with optical data observed, for instance, can contribute to improving our understanding of those carries and the PAH chemistry in the Universe.

In this paper, we combined optical and infrared data of a sample of Sy and SB galaxies to characterize the main type of PAH molecules present in these objects and the local physical conditions of their irradiating sources, as well as the characteristics of the residing ionized gas. The paper is organized as follows. In Section 2, we describe the selection of our sample and the data utilized. In the Sections 3 and 4, the data analysis is presented. The results and discussions are given in Section 5. The conclusion of the outcome is presented in Section 6.

2 OBSERVATIONAL DATA AND SAMPLE DESCRIPTION

We compiled from the literature a sample of Sy and SB galaxies with observed and reduced spectra in the infrared and optical. We selected all SB and Sy galaxies with redshift lower than 0.04 from the Spitzer/IRS ATLAS project[1] (Hernán-Caballero & Hatziminaoglou 2011) and with low-resolution ($R \sim 100$) spectra in the range from 5 to 15 μm, obtained with the Infrared Spectrograph (IRS; Houck et al. 2004) instrument on board the *Sptizer Space Telescope* (Werner et al. 2004). From this preliminary sample, we chose only objects with optical spectra in the Sloan Digital Sky Survey (SDSS) DR16 (Ahumada et al. 2019). Also, all the selected spectra approximately correspond to nuclear region of the galaxies. All the infrared spectra were obtained in staring-mode, except for Buchanan et al. (2006) and Wu et al. (2009), who utilized the spectral mapping mode, but only the nuclear spectrum was given. We used short-low spectroscopy module covering interval between 5.2 μm and 14.5 μm with a resolving power of $R \sim$ 60–127 and slit size of 3.6–3.7 arcseconds per 57 arcseconds.

Table 1 lists the objects selected for this study, including some basic features. The ionizing source of each galaxy was initially taken from the literature. Diagnostic diagrams initially proposed by Baldwin, Phillips & Terlevich (1981) (e.g. [O III]/Hβ versus [N II]/Hα, [O III]/Hβ versus [S II]/Hα, and [O III]/Hβ versus [O I]/Hα), which are commonly known as BPT diagrams are used to distinguish objects ionized by massive stars (SFs), AGN, and low-ionization nuclear emission-line regions (LINERs). In order to verify the classification of the ionizing source of our sample, we show in Fig. 1 the diagram [O III]/Hβ versus [N II]/Hα. The black solid curve represents the theoretical upper limit for the star-forming regions proposed by Kewley et al. (2001) and the black dashed curve is the empirical star-forming limit proposed by Kauffmann et al. (2003), hereafter Ke01 and Ka03, respectively. The blue dot–dashed curve represents the Sy-LINER dividing line (Ke01). According to Fig. 1, some galaxies presented a different classification from the literature. However, the nuclear region of the galaxies of our sample is ionized by AGN, including the galaxies that are between Ke01 and Ka03 lines, region denominated as composite region, where the object is ionized by SF and AGN. Then, throughout the text, we will refer to our sample of galaxies as AGNs.

The optical data compiled from SDSS were obtained with BOSS Spectrograph attached to 2.5-m telescope at Apache Point Observatory. The spectra range considered is between 3600 and 10 400 Å, spectral resolution of $R = 1\,560$ at 3700 Å, $R = 2270$ at 6000 Å and the fiber diameter is 3 arcsec.

Fig. 2 shows an optical spectrum of the nuclear region of the SB galaxy NGC 4676, where some emission lines are highlighted, and an infrared spectrum for the same galaxy with the main bands of PAHs indicated. All the compiled spectra were reduced and calibrated in flux and wavelength.

3 OPTICAL DATA ANALYSIS

The optical spectra from SDSS within the wavelength range of 3600–10400 Å were used to estimate some physical properties of the ionized gas through the use of emission line intensity ratios in combination with photoionization models. The spectrum of each galaxy was processed following the steps listed below:

[1] http://www.denebola.org/atlas/

Table 1. Selected objects and their respective information, including the source's name, IR reference, nuclear type, equatorial coordinates (α and δ), absolute magnitude in visual band (M_B), bolometric luminosity in visual band (L_V), and infrared luminosity L_{IR}.

Object	IR Reference	Nuclear Type	$\alpha(2000)^a$	$\delta(2000)^a$	z^a	$M_B(\mathrm{mag})^a$	$L_V\ (L_\odot)^a$	$L_{IR}\ (L_\odot)^a$
Mrk 273	Wu et al. (2009)	Seyfert [1]	$13^h44^m42^s.1$	$55^h53^m13^s.0$	0.038	−22.34	8.37×10^{10}	7.94×10^{10}
MrK 471	Deo et al. (2007)	Seyfert [1]	$14^h22^m55^s.4$	$32^h51^m03^s.0$	0.034	−22.80	4.58×10^{10}	4.21×10^{10}
Mrk 609	Deo et al. (2007)	Seyfert [1]	$03^h25^m25^s.3$	$-06^h08^m38^s.0$	0.034	−22.48	6.58×10^{10}	4.85×10^{10}
Mrk 622	Deo et al. (2007)	Seyfert [1]	$08^h07^m41^s.0$	$39^h00^m15^s.0$	0.029	−21.44	3.18×10^{10}	1.85×10^{10}
Mrk 883	Deo et al. (2007)	Seyfert [1]	$16^h29^m52^s.9$	$24^h26^m38^s.0$	0.038	−22.19	2.70×10^{10}	3.95×10^{10}
NGC 660	Brandl et al. (2006)	LINER [1]	$01^h43^m02^s.4$	$13^h38^m44^s.4$	0.003	−21.50	1.32×10^{10}	2.02×10^{10}
NGC 2622	Deo et al. (2007)	Seyfert [5]	$08^h38^m10^s.9$	$24^h53^m43^s.0$	0.023	−22.80	4.75×10^{10}	6.35×10^{10}
NGC 2623	Brandl et al. (2006)	Starburst [2]	$08^h38^m24^s.1$	$25^h45^m16^s.9$	0.018	−21.80	3.35×10^{10}	1.74×10^{11}
NGC 4676	Brandl et al. (2006)	Starburst [3]	$12^h46^m10^s.1$	$30^h43^m55^s.0$	0.009	−20.97	2.20×10^{10}	5.15×10^{10}
NGC 4922	Wu et al. (2009)	Seyfert [4]	$13^h01^m24^s.9$	$29^h18^m40^s.0$	0.024	−22.20	2.75×10^{10}	–
NGC 5256	Wu et al. (2009)	Seyfert [4]	$13^h38^m17^s.5$	$48^h16^m37^s.0$	0.028	−22.85	5.23×10^{10}	1.06×10^{11}
NGC 5347	Buchanan et al. (2006)	Seyfert [1]	$13^h53^m17^s.8$	$33^h29^m27^s.0$	0.008	−20.33	4.65×10^{9}	3.43×10^{9}

Notes. References: [1] Veron-Cetty & Veron (2003); [2] Keel (1984); [3] Liu & Kennicutt (1995) [4] Rush, Malkan & Spinoglio (1993); [5] Deo et al. (2007).
[a]Taken from the NASA Extragalactic Database (NED).

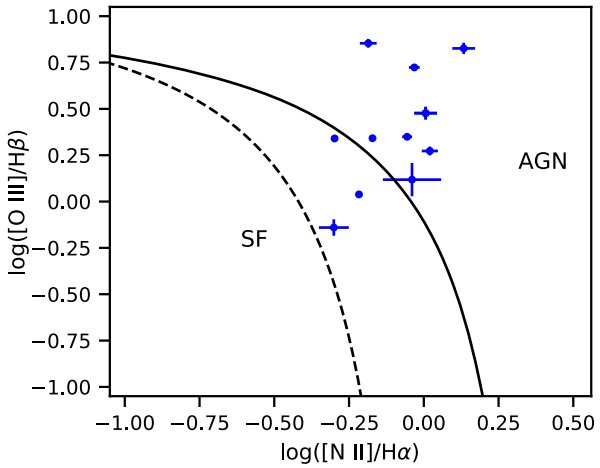

Figure 1. [O III]/Hα versus [N II]/Hα diagnostic diagram for galaxies of our sample. The black solid curve represents the theoretical upper limit for the star-forming regions proposed by Ke01, and the black dashed curve is the empirical star-forming limit proposed by Ka03. The region between the Ke01 and Ka03 lines is denominated composite region.

(i) The spectra were corrected to their rest-frame, adopting the values of z listed in Table 1.

(ii) The pure nebular spectra were obtained after the subtraction of stellar population contribution of the observed spectrum. To obtain the stellar population contribution, we use the stellar population synthesis code STARLIGHT developed by Cid Fernandes et al. (2005) Mateus et al. (2006), and Asari et al. (2007). The code fits an observed spectrum with a combination of simple stellar population (SSP) models excluding the emission lines and spurious features (bad pixels or sky residuals). We use the spectral basis of Bruzual & Charlot (2003) with 45 synthetic SSPs spectra with three metallicities, Z = [0.2, 1, and 2.5] $Z_\odot$, and 15 ages, t = [0.01, 0.003, 0.005, 0.01, 0.025, 0.04, 0.1, 0.3, 0.6, 0.9, 1.4, 2.5, 5, 11, and 13] $\times\ 10^9$ yr. The synthetic SSP spectra have a spectral resolution of 3 Å and to obtain the same spectral resolution of observed spectra these were blended with an elliptical Gaussian function. For more details about the synthesis method, see Cid Fernandes et al. (2005), Mateus et al. (2006), and Asari et al. (2007). The flux of the lines in the pure nebular spectra was measuring by using in-house fitting code, which fitting gaussian functions to the line profiles (Hernandez-Jimenez et al. 2013, 2015).

(iii) The residual extinction associated with the gaseous component for each galaxy was calculated by comparing the observational value for Hα/Hβ ratio to the theoretical value of 2.86 obtained by Hummer & Storey (1987) for the Case B at electron temperature and density of 10 000 K and 100 cm^{-3}, respectively. For this, the following expression was considered

$$\frac{I(\lambda)}{I(\mathrm{H}\beta)} = \frac{F(\lambda)}{\mathrm{F}(\mathrm{H}\beta)} \times 10^{c(\mathrm{H}\beta)[f(\lambda)-f(\mathrm{H}\beta)]}, \quad (1)$$

where $I(\lambda)$ is the intensity (reddening corrected) of the emission line at a given wavelength λ, $F(\lambda)$ is the observed flux of the emission line, $f(\lambda)$ is the adopted reddening curve normalized to Hβ, and $c(\mathrm{H}\beta)$ is the interstellar extinction coefficient.

Table 2 lists the reddening function $f(\lambda)$, the reddening corrected emission line intensities $I(\lambda)$, and the logarithmic extinction coefficient $c(\mathrm{H}\beta)$ for each object.

3.1 Oxygen abundance and ionization parameter

This section briefly discusses the methods used to estimate the oxygen abundance and the ionization parameter of the ionized gas in the galaxies.

Oxygen is the element widely used as a proxy for global gas-phase metallicity Z (Kennicutt, Bresolin & Garnett 2003; Hägele et al. 2008) of gaseous nebulae. This element has prominent emission lines; and their most important ionization stages are present in the optical spectra of these objects. One of the most reliable methods to determine the oxygen abundance is based on the ratio between oxygen forbidden lines and hydrogen lines, and the electron temperature (T_e), specially for star-forming regions and planetary nebulae. Measurements of the auroral lines, such as [O III] λ 4363, and [N II] λ 5755, are necessary to determine T_e. Unfortunately, they are very faint and often drop below the detectability level in the spectra of high-metallicity H II regions. This method is known as the T_e-method or direct method. Unfortunately, we do not detect temperature-sensitive emission lines [O III] λ 4363, and [N II] λ 5755 in the spectra of the galaxies, and then the direct method could not be used to determine the O/H abundance.

Here, we determine the O/H abundance combining the observed emission line ratios with a grid of photoionization models. The

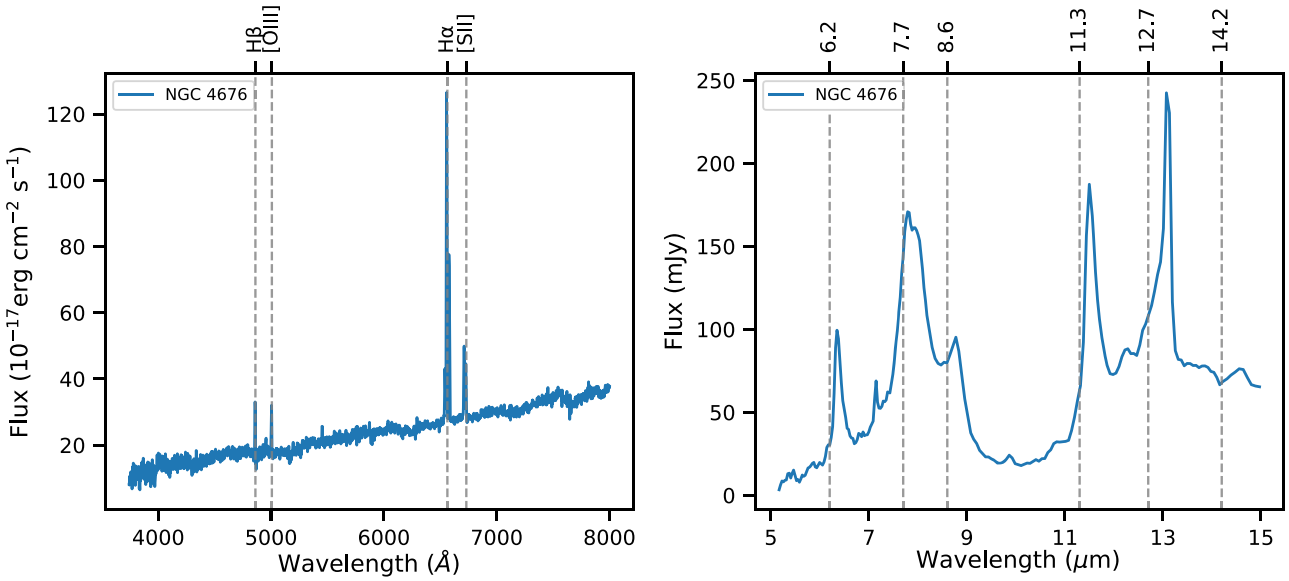

Figure 2. Left-hand panel: the observed optical spectrum for the nuclear region of NGC 4676 obtained with SDSS. Right-hand panel: the observed infrared spectrum for the nuclear region of NGC 4676 obtained with IRS of Spitzer.

Table 2. Reddening corrected emission-line intensities and the logarithmic extinction coefficient, $c(\mathrm{H}\,\beta)$. The flux for H β and H α are 100 and 286, respectively.

Object $f(\lambda)$	[O III] λ4959 −0.02	[O III] λ5007 −0.04	[N II] λ6548 −0.35	[N II] λ6584 −0.39	[S II] λ6716 −0.39	[S II] λ6731 −0.43	$c(\mathrm{H}\,\beta)$
MrK 273	77 ± 2	224 ± 5	87 ± 2	252 ± 7	79 ± 2	65 ± 2	1.29 ± 0.02
Mrk 471	226 ± 10	670 ± 28	131 ± 9	389 ± 24	96 ± 8	84 ± 7	0.69 ± 0.05
Mrk 609	178 ± 4	529 ± 11	90 ± 3	266 ± 8	49 ± 2	52 ± 3	0.67 ± 0.03
Mrk 622	101 ± 9	300 ± 15	98 ± 6	290 ± 18	65 ± 4	56 ± 4	0.67 ± 0.05
Mrk 883	73 ± 1	219 ± 1	48 ± 1	144 ± 2	74 ± 1	58 ± 1	0.39 ± 0.01
NGC 660	66 ± 4	187 ± 6	105 ± 5	300 ± 13	75 ± 3	58 ± 3	1.55 ± 0.04
NGC 2622	310 ± 8	947 ± 23	186 ± 9	569 ± 23	175 ± 10	184 ± 11	0.04 ± 0.04
NGC 2623	46 ± 6	131 ± 18	91 ± 14	261 ± 41	75 ± 12	58 ± 9	1.30 ± 0.14
NGC 4676	25 ± 3	72 ± 5	50 ± 4	143 ± 12	63 ± 5	44 ± 4	1.29 ± 0.07
NGC 4922	75 ± 1	220 ± 2	66 ± 1	193 ± 3	50 ± 1	48 ± 1	1.00 ± 0.01
NGC 5256	37 ± 1	109 ± 1	58 ± 1	174 ± 1	63 ± 1	58 ± 1	0.53 ± 0.01
NGC 5347	239 ± 8	714 ± 23	62 ± 3	186 ± 9	75 ± 4	66 ± 4	0.55 ± 0.04

photoionization model grids were built using version 17.02 of the CLOUDY code (Ferland et al. 2017) in order to compare the observational emission-line intensity ratios for the galaxies in our sample with the photoionization model predictions for similar emission-line intensity ratios. The input parameters of the models are briefly described in the following, however, for more details to these parameters, see Dors et al. (2015, 2017, 2020) and (Carvalho et al.).

(i) The spectral energy distribution (SED): The SED utilized was typical of AGNs, consisting of the sum from the Big Bump component peaking at ≈1 Ryd, which is parametrized by the temperature of the bump assumed to be 1.5×10^5 K and, an X-ray power law with spectral index $\alpha_x = -1.0$, representing the non-thermal X-ray radiation. The continuum between 2 keV and 2500 Å is described by a power law with the optical to X-ray spectral index α_{ox}, which is defined by

$$\alpha_{ox} = \frac{\log[F(2\,\mathrm{keV})/F(2500\,\text{Å})]}{\log[\nu(2\,\mathrm{keV})/\nu(2500\,\text{Å})]}, \quad (2)$$

where F is the flux at 2 keV, 2500 Å, and ν are the corresponding frequencies (Tananbaum et al. 1979). Therefore, the α_{ox} is the power-law slope connecting the monochromatic flux at 2500 Å and at 2 keV and display hard X-ray spectra. For instance, SEDs with small values of α_{ox}, e.g −2, represent an ionization source with a very soft spectrum yielding models with a very low ionization degree (e.g. Dors et al. 2019).

(ii) Metallicity (Z): The metallicities used in relation with the solar value ($Z/Z_\odot$) was 0.5, 1.0, 1.5, 2.0, 2.5, 3.0, 3.5, and 4.0. The assumed solar oxygen abundance is $12 + \log(\mathrm{O/H})_\odot = 8.69$ (Prieto, Lambert & Asplund 2001; Asplund et al. 2009) whose abundances 8.40, 8.69, 8.86, 8.99, 9.08, 9.16, 9.23, and 9.29, correspond to the above listed metallicities, respectively.

(iii) Ionization parameter (U): The ionization parameter is defined by $U = Q(\mathrm{H})/4\pi R_0^2 nc$, where the Q(H) is the number of ionizing photons emitted per second by the ionizing source, R_0 is the distance from the ionization source to the inner surface of the ionized gas cloud in cm, n [cm^{-3}] is the total hydrogen density (ionized, neutral, and molecular), and c is the speed of light in km s^{-1}. We considered the logarithm of U in the range of $-4.0 \leq \log U \leq -1$, about the

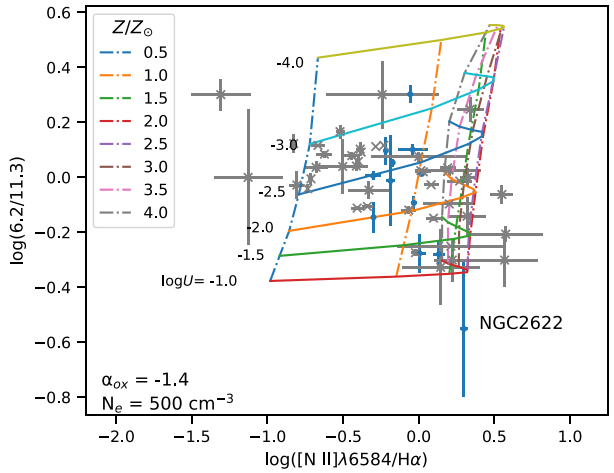

Figure 3. Log(6.2/11.3) versus log([N II] λ6584/H α) diagram. Dashed lines connect photoionization model results with the same metallicity, while solid lines connect models with the same logarithm of the ionization parameter U, as indicated. The blue points represent the observational line intensity ratios from the sample considered in this work; and the grey points represent data from Smith et al. (2007). The assumed values of the metallicity ($Z/Z_\odot$) and log U values are indicated.

same values considered by Feltre, Charlot & Gutkin (2016) for AGNs.

(iv) Electron density: We assumed for the models an electron density value of $N_e = 500\,cm^{-3}$, constant in the nebular radius. The electron density (N_e) derived from the [S II] λ 6717/λ 6731 for our sample of galaxies is in the range of 111 to 922 cm^{-3}, with a mean density of $N_e = 411\,cm^{-3}$.

(v) Inner and outer radius: The inner radius of 3 pc was assumed, which is the distance from the ionizing source to the illuminated gas region. It is a typical value for Sy galaxies (Balmaverde et al. 2016). The outer radius was assumed to be the one where the electron temperature of the gas reaches 150 K. It is worth mentioning that studies have found pieces of evidence that the inner wall of the dust torus has around several tenths of a parsec from the central engine (e.g. Xie, Li & Hao 2017). However, models with different combinations of Q(H), inner radius, and N_e that result in the same U are homologous models with about the same predicted emission-line intensities (Bresolin, Kennicutt & Garnett 1999; Dors et al.).

(vi) PAH: The size distribution for PAHs is given by a power law of the form $a^{-3.5}$, where a is the PAH radius and the number of carbon atoms range from 30 to 500, and 10 size bins (Abel et al. 2008).

In order to extend this analysis to other sources with a wider range of metallicities, we included data taken from the sample of the Spitzer Infrared Nearby Galaxies Survey (SINGs) by Smith et al. (2007), in which the 6.2/11.3 and 6.2/7.7 emission ratios were considered. The log([N II] λ6584/H α) values of this sample were taken from Moustakas et al. (2010). This sample is composed of Sy, LINERS, and star-forming galaxies.

In Fig. 3, a diagram log(6.2/11.3) versus log([N II] λ6584/H α), the observational data and the photoionization model results obtained with the CLOUDY code, assuming $\alpha_{ox} = -1.4$, are shown. It is worth to mention that [N II λ6584/H α line ratio is highly sensitive to the metallicity, as measured by the oxygen abundance (O/H) and has a small (although not negligible) ionization parameter dependence (e.g. Kewley, Nicholls & Sutherland 2019; Carvalho et al. 2020). An opposite behaviour is derived for the log(6.2/11.3), which shows a stronger dependence with the ionization degree of the gas (represented by U) mainly for the highest values of U rather than with the metallicity. We built grid of models with $\alpha_{ox} = -1.1$ and -1.4 and verify that the photoionization model results reproduce the majority of the observed line ratios assuming from the optical to X-ray spectral index $\alpha_{ox} = -1.4$ (see Fig. 3), while for $\alpha_{ox} = -1.1$ (not shown here), there are more points that are not reproduced by the photoionization models. Therefore, we adopted $\alpha_{ox} = -1.4$. This value is representative of typical AGNs, as described in the Hazy manual of the CLOUDY code,[2] and pointed out by Miller et al. (2011), Zhu et al. (2019), and Dors et al. (2019). To calibrate the metallicity as a function of the log(6.2/11.3), we calculated the logarithm of the ionization parameter and the metallicity values for each object of our sample by linear interpolations between the models shown in Fig. 3. Table 3 lists the oxygen abundance and the ionizing parameter U derived by linear interpolation between the models.

Table 3. The oxygen abundance and the ionizing parameter U.

Object	$12 + \log(O/H)_\odot$	$\log(U)$
Mrk 273	8.64 ± 0.01	-3.42 ± 0.11
Mrk 471	8.83 ± 0.03	-1.28 ± 0.23
Mrk 609	8.69 ± 0.02	-2.08 ± 0.08
Mrk 622	8.76 ± 0.04	-1.33 ± 0.33
Mrk 883	8.62 ± 0.02	-2.00 ± 0.33
NGC 660	8.70 ± 0.01	-2.37 ± 0.05
NGC 2622	–	–
NGC 2623	8.67 ± 0.05	-2.62 ± 0.10
NGC 4676	8.60 ± 0.02	-2.49 ± 0.09
NGC 4922	8.63 ± 0.00	-2.55 ± 0.05
NGC 5256	8.61 ± 0.01	-2.69 ± 0.15
NGC 5347	8.64 ± 0.03	-2.35 ± 0.61

4 INFRARED DATA ANALYSIS

4.1 PAHFIT

The mid-IR spectrum of any object is composed of a diversity of components, such as dust and stellar continuum, emission features from PAHs, forbidden spectral lines from Ne, Ar, S, and Fe, and rotational lines from molecular hydrogen. In low-resolution spectra, these components are blended, and it is necessary to separate them. We employed the spectrum fitting tool PAHFIT (Smith et al. 2007) to decompose the 5–15 μm low-resolution Spitzer's IRS spectra and obtain the fluxes for different PAH features from our sample.

The default PAHFIT parameters were adopted in the fitting. The dust continuum was represented by blackbodies at fixed temperatures of T = 35, 40, 50, 65, 90, 135, 200, and 300 K. Drude profiles were applied to recover the full strength of dust emission features, with PAH emissions at central wavelengths of 5.3, 5.7, 6.2, 6.7, 7.4, 7.6, 7.7, 7.8, 8.3, 8.6, 10.7, 11.2, 11.3, 12.0, 12.6, 12.7, 13.5, 14.0, and 14.2 μm. From these measurements, we analysed the emissions of 6.2-μm PAH, 7.7-μm PAH complex, and 11.3- μm PAH complex. The 7.7-μm PAH complex is the sum of 7.6, 7.7, and 7.8 μm, while 11.3-μm PAH complex is the sum of 11.2 and 11.3 μm.

The integrated PAH fluxes analysed in this work are given in Table 4. Fig. 4 shows the detailed decomposition of the SB galaxy NGC 4676 from 5 to 15 μm obtained with the PAHFIT code in the components: total continuum, ionic lines, stellar lines, best-fitting

[2] http://web.physics.ucsb.edu/~phys233/w2014/hazy1_c13.pdf

Table 4. Integrated PAH fluxes (in units of 10^{-16} W m^{-2}) obtained by the PAHFIT code.

Object	6.2 μm	6.7 μm	7.4 μm	7.6 μm	7.8 μm	8.6 μm	11.2 μm	11.3 μm	12.6 μm	12.7 μm
			7.7-μm complex				11.3- μm complex		12.6- μm complex	
MrK 273	39.40	36.70	96.60	51.90	82.80	31.40	12.10	7.53	23.10	2.34
Mrk 471	3.79	0.49	0.06	5.60	5.80	3.28	1.42	5.79	3.54	0.26
Mrk 609	15.20	4.76	9.52	24.40	25.40	14.40	3.52	15.30	8.50	1.33
Mrk 622	3.74	1.45	3.59	5.19	5.52	2.95	2.31	4.76	3.81	0.00
Mrk 883	2.97	0.74	0.36	4.22	3.67	1.77	0.96	3.19	1.57	0.36
NGC 660	263.00	112.00	434.00	322.00	496.00	235.00	39.60	216.00	156.00	23.90
NGC 2622	0.59	0.43	0.00	1.57	1.53	0.56	0.58	1.53	0.23	0.22
NGC 2623	46.80	19.20	93.80	51.10	86.80	50.80	12.70	24.40	30.50	4.03
NGC 4676	21.60	7.49	28.30	27.50	31.50	15.40	6.51	14.80	12.30	1.59
NGC 4922	16.00	8.02	21.60	18.40	21.90	10.10	4.04	10.10	7.13	1.23
NGC 5256	32.10	11.10	54.30	41.30	49.10	23.00	7.18	18.50	19.50	0.54
NGC 5347	7.20	10.00	28.80	2.63	8.32	4.79	0.92	6.49	5.99	0.00

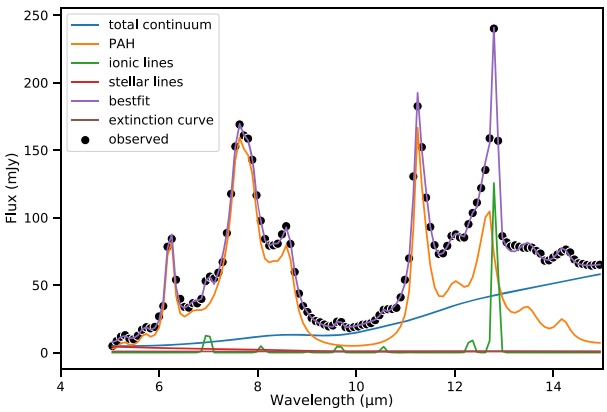

Figure 4. Detailed decomposition of NGC 4676 from 5 to 15 μm obtained with the PAHFIT code in components of the total continuum, ionic lines, stellar stars, the best-fitting model, and PAH features.

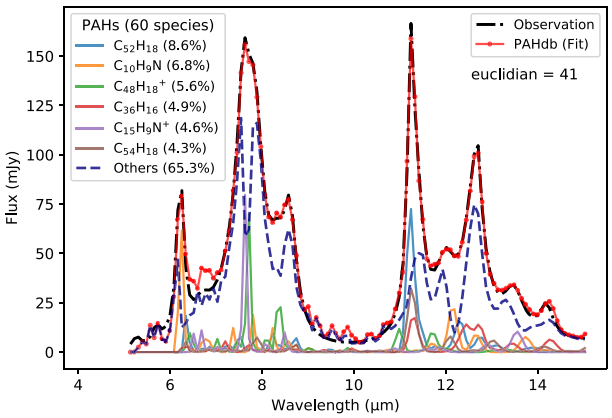

Figure 5. The PAHdb model fitting for the observed spectrum of NGC 4676. The quality of the fitting is quantified by the parameter Euclidean. The fractional contribution to the flux from the species is shown.

model, and PAH features. This spectral decomposition was similarly applied to the other eleven objects in our sample.

4.2 PAH spectra

The PAH spectra of our sample obtained using the PAHFIT were analysed using version 3.2 of the NASA Ames PAH IR Spectroscopic Database (PAHdb; Boersma et al. 2014; Bauschlicher et al. 2018), which contains 4233 theoretically calculated PAH spectra. In order to perform the fit, we used the version online of the PAHdb, which is based on spectra of individual aromatic molecules with specific charge states, structures, compositions, and sizes. The Gaussian line profile with a full width at half-maximum (FWHM) of 15 cm^{-1} and a uniform shift of 15 cm^{-1} for all bands was assumed to mimic some effects of anharmonicity. Fig. 5 illustrates the fitting obtained for the spectrum of NGC 4676, and it shows the main species that are contributing to the IR emission in NGC 4676. This fitting resulted in sixty species contributing to the galaxy's flux. The contributions of the six species that contribute most to the galaxy's flux are in parenthesis and the their adjusts are shown in different colours. In blue, the contribution of all 54 other species. In Fig. 5, it is possible to see the quality of the fit measured by Euclidean norm,[3] whose results are displayed at the top right-hand of the figure. The fitting obtained for the remaining objects is shown in Figs B1 and B2 (see Appendix B).

[3]Euclidean norm is one mathematical method that measures the distance between two points. In this case, the observed and the theoretical ones. Therefore, the lower the Euclidean norm, the better the quality of the fit.

5 RESULTS AND DISCUSSION

5.1 Oxygen abundance and the ionization parameter

The effects of the radiation field and metallicity on the intensity ratios and PAH equivalent widths have been reported by many authors in the literature. Due to the significant radiation field of AGNs as revelead by the presence of a significant hot dust continuum, the small PAHs could be destroyed, which tend to decrease the 6.2 and 11.3-μm intensities (e.g. Sturm et al. 2000; Desai et al. 2007; Diamond-Stanic & Rieke 2010). Smith et al. (2007) performed a study for a sample of Sy, LINER, and star-forming galaxies, and found a trend of the increase of the integrated luminosity of the PAH bands, relative to the total infrared, with the increasing of the oxygen abundance. Besides, these authors verified that the 7.7/11.3 PAH intensity ratio does not vary with the radiation hardness, measured as [Ne III]/[Ne II] for star-forming galaxies, but shows a dependence for AGNs, specially for [Ne III]/[Ne II] > 0.1. However, Maragkoudakis et al. (2018) verified a very weak dependence of the 7.7/6.2 on the hardness of the radiation field and the ionization index for the H I regions along the M 83 and M 33 galaxies (for a review, see for instance, Li 2020).

Fig. 6 presents the 6.2/11.3-μm emission ratio as a function of the oxygen abundance (12 + log(O/H)) and the logarithm of the

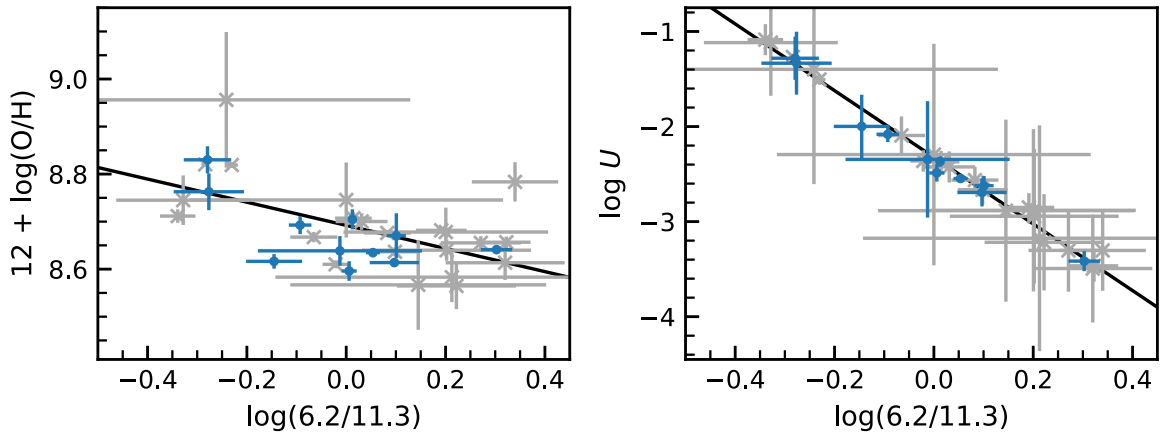

Figure 6. 6.2/11.3 emission ratio as a function of the oxygen abundance (12 + log(O/H)) and the logarithm of the ionization parameter of hydrogen (log U). Blue points represent the galaxies of our sample and grey points the SINGs sample of galaxies from Smith et al. (2007). The black solid line is the linear fit to the data.

ionization parameter of hydrogen (log U) for our sample of galaxies and the SINGs sample by Smith et al. (2007). We notice that the 6.2/11.3-μm PAH intensity presents a linear correlation with the oxygen abundance, and the ionization parameter U. We find the best-fitting line of $12 + \log(\mathrm{O/H}) = -0.24 \times \log(6.2/11.3) + 8.69$, with $R = -0.58$, and $\log(U) = -3.51 \times \log(6.2/11.3) - 2.32$, with a Pearson correlation coefficient of $R = -0.99$. It is important to emphasize, that for the first time, we found that the photoionization models can reproduce most of the observational data in the log (6.2/11.3) versus log([N II] λ6584/H α) diagram.

5.2 Species identification and degeneracy

The knowledge on the physico-chemical conditions of the environments where PAHs and PANHs exist is of great importance to understanding the molecular formation and destruction, with the possibility of new compounds being formed. Many issues have been raised about which aromatic species can be found in space environments, while theoretical studies have been conducted out to determine vibration frequencies of potential candidates (Ricca et al. 2019; Mattioda et al. 2020). Also, understanding the link between the evolutionary stage of environments and the aromatic species in them is an enigma that must be studied. In this work, we will call PANH any aromatic molecule composed of carbon, hydrogen, and nitrogen, whether nitrogen is inside or outside the ring.

The PAH abundances (PAH per cent) for each species, i.e. the percentage of the contribution on the flux of each species to the total flux in the spectral range between 5−15 μm, were obtained by dividing the flux contribution of each species by the total flux, which includes the contributions of all species. The total number of species that contribute to IR emission to each galaxy varies from 49 to 77. These species are presented in Appendix C for the twelve studied objects. The most relevant identified species in the sample contain 10−82 carbon atoms, while the overall species can be composed of 9−170 carbon atoms.

Among the pure hydrocarbons, we highlight the $C_{52}H_{18}$, which is present in 75 per cent of the sample and contributes from about 4–13 per cent in the galaxy's fluxes. Among nitrogenous PAHs, $C_{10}H_9N$ is present in 92 per cent of the sample, with fluxes contributions ranging from about 3–8 per cent. The molecular ion $C_{10}H_9N^+$ is also present in several galaxies analysed in this work. Similar species such as benzonitrile, also called cyanobenzene (C_6H_5CN), and cyanonaphthalenes ($C_{10}H_7N$) have already been detected in the dark molecular cloud TMC-1 (McGuire et al. 2018, 2021; McCarthy & McGuire 2021). Confirmation of hydrocarbons with CN, such as cyanobenzene in TMC-1 and other sources, improves our understanding of chemical processes. Reactions between unsaturated hydrocarbons with CN are usually exothermic and without barrier activation. Furthermore, CN is an abundant radical in most molecular clouds. Since cyan derivatives have significant dipole moments, they are easy targets to detect in radio and, therefore, will have bright rotation spectra (McCarthy & McGuire 2021).

It is known that there is degeneracy in the fitting of the spectra using the PAHdb data base; and it is not possible to guarantee that these three species are always present in the spectra of the galaxies studied here. If $C_{52}H_{18}$, $C_{10}H_9N$, and $C_{14}H_{11}N$ are excluded from the data base, the PAH spectra can still be reproduced, but the quality of the fitting decreases and the Euclidean have a slightly worse result. In this context, it is worthwhile to known that the species $C_{14}H_{11}N$, is simply $C_{10}H_9N$ with the addition of one more aromatic ring. This molecule is present in 60 per cent of the sample, and contributes of 2–6 per cent of the total flux. For example, the fitting of the spectrum of the galaxy Mrk 273 performed using all data base resulted in the contribution of 56 species (see the fitting in Fig. B1), with an Euclidean close to 95. When the species $C_{52}H_{18}$, $C_{10}H_9N$, $C_{14}H_{11}N$, and their isomers (15 species) were removed, the PAHdb resulted in 53 species contributing to the galaxy's flux and the Euclidean value was 108. In this case, some new species were introduced, as well as the relative quantity of the species was slightly modified, when compared with the first fitting (considering all data base). However, these new species have the same characteristics of the excluded species, being, majority, small pure PAHs, or small PAHs with heteroatom (N or O), with two or three fused aromatic rings. Therefore, although excluded molecules are more appropriate, molecules of the same family also reproduce the spectra of the galaxies, and the presence and (relative) quantity of the PAH species is not uniquely determined.

Then, a coarse, but robust description of the contribution of the types of PAHs of a galaxy may be obtained by grouping their different types. We grouped these types according to Andrews et al. (2015), as dehydrogenated, pure, PANHs, and heteroatom. The Table 5 lists the results of flux contribution according to these components.

5.3 PANHs and the Peeter classification

Hudgins et al. (2005) demonstrated that only the nitrogen incorporated into the aromatic rings is capable of reproducing the interstellar

Table 5. Flux contribution grouped by type of PAHs.

Object	Dehydrogenated (per cent)	Pure PAHs (per cent)	PANHs (per cent)	Heteroatom (per cent)
Mrk 273	42.1	25.1	32.5	0.3
Mrk 471	31.5	53.3	11.9	3.4
Mrk 609	32.2	55.3	10.4	2.0
Mrk 622	36.2	48.9	10.8	4.2
Mrk 883	28.6	60.0	8.3	3.1
NGC 660	33.8	44.3	19.0	3.0
NGC 2622	37.3	51.1	10.8	0.8
NGC 2623	35.2	41.4	23.4	0.0
NGC 4676	30.2	48.9	19.9	1.1
NGC 4992	32.0	49.9	15.9	2.2
NGC 5256	31.6	48.6	19.4	0.4
NGC 5347	47.8	36.2	15.1	1.3

Table 6. Peeters' classification of the 6.2-, 7.7-, and 8.6-μm PAH bands of the studied galaxies.

Source	6.2 μm Class	7.7 μm Class	8.6 μm Class	Reference
Mrk 273	A	B	A	[1,2]
MrK 471	B	A	B	[1,2]
Mrk 609	A	B	B	[1,2]
MrK 622	A	A	A	[1,2]
Mrk 883	B	A	A	[1,2]
NGC 660	A	A	A	[1,2]
NGC 2622	B	A	A	This work
NGC 2623	A	B	B	[1,2]
NGC 4676	A	B	A	[1,2]
NGC 4922	A	A	B	This work
NGC 5256	A	A	B	[1,2]
NGC 5347	B	C	–	This work

Notes. References: [1] Canelo et al. (2018); [2] (Canelo et al. 2021).

observations of the 6.2-μm PAH band at shorter wavelengths through experimental process. The blueshift of the 6.2-μm band was also observed in 67 per cent of 155 SB-dominated galaxies (Canelo et al. 2018). Moreover, Boersma, Bregman & Allamandola (2013) proposed that the PANH cations dominate both the 6.2- and 11.0-μm emissions in slightly dense regions of the photodissociation region (PDR) known as NGC 7023, and they are also significantly responsible for the emissions of the 7.7, 8.6, 12.0, and 12.7 μm features.

PANHs, both neutral and cation, generate up to 55 per cent of emission at 6.2 μm in our sample of galaxies . PANHs also contribute, on average, about 5.7 per cent of the band flux in 11.3 μm, reaching the value of 37 per cent in the MRK 883.

The importance of N-containing PAHs in the total emission of our sample is also in agreement with the results obtained by Canelo et al. (2018, 2021), as can be seen in Table 6. This table shows the Peeters' classification of the 6.2, 7.7, and 8.6 μm bands (Peeters et al. 2002), previously obtained by Canelo (2020) to most of our galaxies together with our current classification for NGC 2622, NGC 4922, and NGC 5347. The procedure for this analysis, as well as the new results from those three sources, are described in Appendix D. The 6.2-μm band, in particular, was mainly distributed into the A class objects, implying a predominance of blue shifted profiles, which are typical of PANH emission and thus confirms the presence of such molecules in these sources.

Besides, we found that the majority of the PAH population is composed of up to 95 per cent of small species[4] (81 per cent being the average) and 79 per cent of neutral PAHs (68 per cent the average) in our sample of galaxies. These values are consistent with those provided by Martins-Franco & Menéndez-Delmestre (2021), who found that the predictions by the code PAHdb species of a sample based on Spitzer/IRS mid-infrared spectra of 700 dusty galaxies from the GOALS and ATLAS surveys shown themselves to be predominantly small and neutral PAHs.

In this sense, we can attribute a young object profile to our studied sources with ISM-type environments and a PAH population dominated by small species (Shannon & Boersma 2019). Therefore, the spectra of our sample are consistent with Peeters' A class object, which corresponds to H II regions and the general material illuminated by a star in the ISM. On the other hand, large PAHs are normally more connected with B class spectra of evolved objects, such as circumstellar material, planetary nebula, and a variety of post-AGB (asymptotic giant branch) stars (e.g Tielens 2008; Andrews et al. 2015; Peeters et al. 2017). Moreover, the B class profiles could also be a mixture of PANH, small and large PAH emissions (Peeters et al. 2002). It is important to note that Yang et al. (2017) suggested that neither PAHs with a large side chain nor PAHs with unsaturated alkyl chains are expected to be present in the ISM in a large abundance. From Table 6, both A and B classes are present in our sample, which emphasizes the importance of spatially resolved observations in the determinations of which locations in the galaxies where those different PAH populations are more relevant.

Furthermore, Boersma et al. (2013) and Andrews et al. (2015) showed that the dominance of the emissions of small molecules increases with the proximity of the ionizing source. Draine & Li (2001) also demonstrated this behaviour when they proposed that small PAHs emit mainly at 6.2- and 7.7-μm bands, while large PAHs emit at longer wavelengths (Allamandola, Hudgins & Sandford 1999). Concerning the neutral species, their predominance is also expected in photodissociation regions where the species can be shielded due to high density/low temperature environments. In fact, Allamandola et al. (1999) demonstrated that the absorption spectrum produced by the neutral PAHs, compared to the spectrum produced by the same PAHs in the cationic form, segregate separately in different regions of the IR when these PAHs are small. According to Bauschlicher, Peeters & Allamandola (2008), small PAHs emit at 5–9 μm region while the emissions at shorter wavelengths of the 11.3-μm profile would be produced by neutral PAH molecules.

5.4 Small and ionized PAHS, PANHS and the ionization parameter

It is widely known that the size of PAH species and their ionization states can directly be related to the physical conditions of the local environment (Tielens 2005; Sidhu et al. 2020), in specially of the ionizing field; and a factor of its characterization is the ionization parameter log U.

In this section, we investigate the relation among the contribution of small PAHs, PANHs and ionized PAHs and log U. In Fig. 7, we plot these PAH populations as a function of ionization parameter. We can see that the contribution of the small PAHs and PANHs drops as the hydrogen ionization parameter increases (left-hand panel). The correlation is very strong in both cases; with a Pearson coefficient

[4]In this work, small PAHs are considered to have a number of carbon atoms lower than 50 ($N_C < 50$), while large PAHs contain $N_C \geq 50$ atoms.

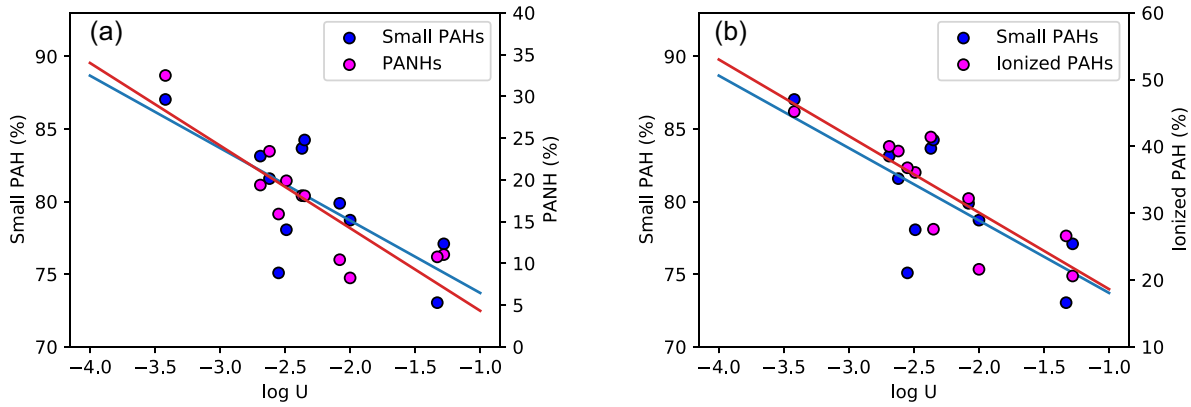

Figure 7. Small PAHs and PANHs versus log U (right-hand) and small PAHs versus log U (left-hand). The red and blue solid lines represent the best fits between the percentage total flux of the species (small, ionized PAHs, and PANHs) and log$U$.

of $R = -0.71$ (P-value=0.012) for the PAHs, while the PANHs has a $R = -0.86$ (P-value=0.0006). The best linear fit for the former molecules is $\text{Flux}_{(\text{SmallPAHs})} = -4.9 \log(U) + 68.76$, whereas for the latter ones is Flux(PANHs) $= -9.9 \log U - 5$. The main reason for a decrease of the fraction of smaller PAHs and PANHs with increasing ionization factor is due to the fact that the latter factor is directly correlated with the rising of the fragmentation rate of the smaller PAHs and PANHs,[5] since they have lower energy of dissociation than larger PAHs (e.g. Peeters et al. 2005). For example, the dissociation energy for the formation of the cation C_3H_3 from the smaller PAH Naphthalene ($C_{10}H_8$) and aromatic hydrocarbon Benzene (C_6H_6) is 19 and 14 eV, respectively (NIST webbook[6]). In addition, the dissociation energy is lower for PANHs than for smaller PAHs (e.g. for dissociation of aromatic hydrocarbon 2-Methylpyridine, C_6H_7N, in the cation C_5H_6 the energy is 12.87 eV), and as most of PANHs in our sample are amides (an amide group outside the ring), the dissociation energy is even lower (e.g. for dissociation of aromatic hydrocarbon Aniline, C_6H_7N, in the cation C_5H_6 the mean energy is 11.96 eV); this explains why the fraction of the smaller PANHs fall (∼35 to ∼5 per cent) faster than the PAHs (∼90 to ∼75 per cent). Likewise, the lower percentage of PANHs (mean value of 17 per cent) with respect to small PAHs (81 per cent) could be explained by their higher rates of dissociation reducing their half-lifetime (Peeters et al. 2005). Therefore, the fraction of small PAHs and PANHs fall as the U factor increases.

According to O'Dowd et al. (2009), an AGN source preferentially destroys small PAH species with its strong radiation field, favouring the predominance of large species. As a consequence, the environment is more metallically enriched due to the high destruction of small PAHs. The studies by Sales et al. (2010) suggested that Sys tend to present an IR emission dominated by PAH molecules with more than 180 carbon atoms, while other objects such as SBs normally form molecules with less than 180 carbons. Indeed, the torus can also explain the dominance of the smaller PAHs in our sample, once it can protect the ISM-type environments of galaxies of our sample of the harder radiation field of the central engine. As can be noted, despite of the presence of the AGN these galaxies were

[5]Most of PANHs found in our sample have $N_C < 50$, except for NGC 5347, MRK 622, and NGC 4676 have the isomers $C_{52}H_{18}N_2^+$ (ID = 258), and $C_{52}H_{18}N_2^{2+}$ (ID = 257), but all them have contributions $\lesssim 1$ per cent.
[6]https://webbook.nist.gov/chemistry/

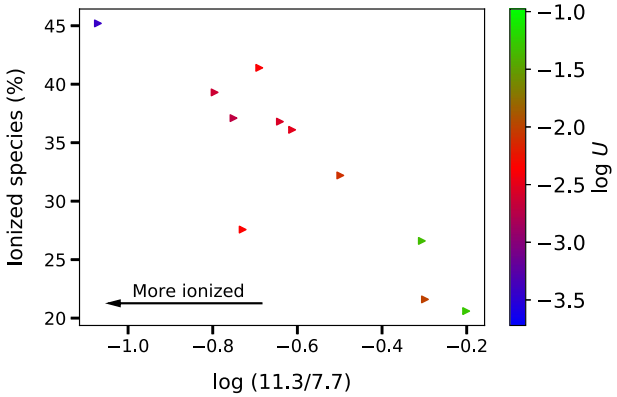

Figure 8. The 11.3/7.7 emission ratios versus ionized species in percentage and log U.

classified as SB-dominated sources, in which class A and B profiles and, consequently, smaller PAHs seem to be presented (e.g. Canelo et al. 2021; Sales et al. 2010, 2013).

The right-hand panel of Fig. 7 also shows that the fraction of ionization of the PAHs decreases as the ionization factor increases. The correlation coefficient is $R = -0.84$ (P-value = 0.001), and the best liner fit is given by Flux(ionized PAHs) $= -11.4 \log U + 7.2$. This result could be explained whether the PAH fragmentation rate is greater than the ionization rate, then, in this case, the percentage of ionized small PAHs diminishes as the U factor increases. Moreover, Jochims et al. (1994) showed that PAHs containing less than 30–40 carbon atoms, when photoexcited, tend to dissociate rather than relax by infrared emission. In the case of larger PAHs, the main relaxation way will occur via infrared emission (see also Sales et al. 2010, 2013).

In order to verify whether our results agrees with the classical models from Draine & Li (2001), we verified the relation between the percentage of ionization of PAHs determined from the PAHdb with the 11.3/7.7 PAH band strength (observational) and the ionization parameter determined from the photoionization models. It is shown in Fig. 8, and as expected, we see that the ionization degree of PAH species increases with the decreasing of the 11.3/7.7 ratio and the ionization parameter. We found that the Ionized species (per cent) = $-28.11 \log(11.3/7.7) + 16.22$, with $R = -0.90$ (P-value = 0.0002).

6 CONCLUSIONS

In this study, we combined optical and infrared data of a sample of Sy and SB galaxies to characterize the main type of PAH molecules present in these objects and the local physical conditions of their irradiating sources, as well as the characteristics of the residing ionized gas. The infrared data were selected from ATLAS Spitzer/IRS with low-resolution spectra in the 5–15 μm wavelength range and local redshift, and the optical spectra from the Sloan Digital Sky Survey, DR16, in the wavelength range of 3600–10 400 Å. Photoionization model grids were built using the CLOUDY code version 17.02 in order to compare the observational emission-line intensity ratios for the galaxies in our sample with the photoionization model predictions for similar emission-line intensity ratios. The main findings are summarized in the following bulletin:

(i) Species containing 10−82 carbon atoms are the most abundant in the sample, while the overall species can be composed of 9−170 carbons.

(ii) Depending on the galaxy in our sample, the PAH population can contain up to 95 per cent of small species (the average being 81 per cent) and 79 per cent of neutral PAHs (the average being 68 per cent).

(iii) Among the pure hydrocarbons, $C_{52}H_{18}$ deserves the most attention, since it is found in 75 per cent of the sample, contributing from about 5–13 per cent in the galaxy's fluxes.

(iv) Concerning PANHs, these species contribute about 8−32 per cent of the total emission in all the studied objects (17 per cent on average). Aromatic amides, such as $C_{10}H_9N$, $C_{10}H_9N^+$, $C_{14}H_{11}N$ and, $C_{15}H_9N^+$ are among the most relevant species contributing to the IR emitting flux. $C_{10}H_9N$ is an important species, which is present in 92 per cent of our sample.

(v) Although it is not possible to guarantee that the aromatic amides mentioned above and $C_{52}H_{18}$ are always present in the spectra of the galaxies studied here, due to degeneracy, the removal of these molecules showed a worsening in the fit and the addition of molecules from the same family (small PAHs and aromatic amides, plus a small addition of Oxy-PAHs), suggesting that small PANHs are responsible for a large part of the emission of the galaxies in the sample. Thus, we suggest that aromatic amides, as well as theirs cations should be considered in future experimental/theoretical studies and observations, intending to search for their interstellar detection at radio wavelengths.

(vi) For the first time, we show the AGN photoionization models with $\alpha_{ox} = -1.4$, reproducing very well the observed data points in the diagram log(6.2/11.3) versus log([N II] λ6584/H α).

(vii) The 6.2/11.3 PAH intensity ratio presents a linear anti correlation between the oxygen abundance and log *U*, in the sense that the 6.2/11.3 ratio decreases as the oxygen abundance and log *U* increases.

(viii) In our sample, the small PAH flux, as well as the ionized PAH and PANH fluxes, exhibit a decrease trend as hydrogen ionization parameter increases. Notice a linear anti correlation between these parameter. We suggest that this behaviour is directly correlated with the rising of the fragmentation rate of the smaller PAHs and PANHs at high U, since they have lower energy of dissociation than larger PAHs. In addition, the dissociation energy is lower for PANHs than for smaller PAHs, according to the observed behaviour, where the fraction of the smaller PANHs fall (35 to 5 per cent) faster than the PAHs (90 to 75 per cent) at the considered log(U) range. On the other hand, the decreasing of ionized PAHs with the increasing of U factor could be explained whether the PAH fragmentation rate is greater than the ionization rate.

(ix) We found that the ionization degree of PAH species increases with the decreasing of the 11.3/7.7 ratio and the ionization parameter (log *U*), in agreement with the models proposed by Draine & Li (2001).

ACKNOWLEDGEMENTS

AS-R acknowledges support from Coordenação de Aperfeiçoamento de Pessoal de Nível Superior (CAPES) and Dr Christiaan Boersma for all assistance provided in using the PAHdb tools. ACK acknowledges support from Conselho Nacional de Desenvolvimento Científico e Tecnológico (CNPq) and Fundação de Amparo à Pesquisa do Estado de São Paulo (FAPESP), process number 2020/16416-5. CMC acknowledges the support of CNPq, process number 141714/2016-6, and CAPES - Finance Code 001. DPPA acknowledges support from CNPq and Fundação de Amparo à Pesquisa do Estado do Rio de Janeiro (FAPERJ). DAS acknowledges support from CNPq and Fundação de Amparo à Pesquisa do Estado do Rio Grande do Sul (FAPERGS). JAHJ acknowledges support from FAPESP, process number 2021/08920-8.

DATA AVAILABILITY

The data underlying this article will be shared on reasonable request to the corresponding author.

REFERENCES

Abel N., Van Hoof P., Shaw G., Ferland G. J., Elwert T., 2008, ApJ, 686, 1125
Ahumada R. et al., 2020, AJSS, 249, 1
Allamandola L., Hudgins D., Sandford S., 1999, ApJ, 511, L115
Alonso-Herrero A. et al., 2014, MNRAS, 443, 2766
Andrews H., Boersma C., Werner M., Livingston J., Allamandola L., Tielens A., 2015, ApJ, 807, 99
Asari N. et al., 2007, MNRAS, 381, 263
Asplund M., Grevesse N., Sauval A. J., Scott P., 2009, ARA&A, 47, 481
Baldwin J. A., Phillips M. M., Terlevich R., 1981, PASP, 93, 5
Balmaverde B., Capetti A., Moisio D., Baldi R. D., Marconi A., 2016, A&A, 586, A48
Bauschlicher C. W., Jr., Peeters E., Allamandola L. J., 2008, ApJ, 678, 316
Bauschlicher C. W., Jr., Ricca A., Boersma C., Allamandola L., 2018, ApJS, 234, 32
Boersma C. et al., 2014, ApJS, 211, 8
Boersma C., Bregman J., Allamandola L., 2013, ApJ, 769, 117
Brandl B. et al., 2006, ApJ, 653, 1129
Bresolin F., Kennicutt R. C., Jr., Garnett D. R., 1999, ApJ, 510, 104
Bruzual G., Charlot S., 2003, MNRAS, 344, 1000
Buchanan C. L., Gallimore J. F., O'dea C. P., Baum S. A., Axon D. J., Robinson A., Elitzur M., Elvis M., 2006, AJ, 132, 401
Campbell E. K., Holz M., Gerlich D., Maier J. P., 2015, Nature, 523, 322
Candian A., Zhen J., Tielens A. G., 2019, Phys. Today, 71, 38
Canelo C. M., 2020, PhD thesis, IAG-USP
Canelo C. M., Friaça A. C., Sales D. A., Pastoriza M. G., Ruschel-Dutra D., 2018, MNRAS, 475, 3746
Canelo C. M., Sales D. A., Friaça A. C. S., Pastoriza M., Menéndez-Delmestre K., 2021, MNRAS, 507, 6177
Carvalho S. P. et al., 2020, MNRAS, 492, 5675
Chen T., 2018, ApJ, 866, 113
Cid Fernandes R., Mateus A., Sodré L., Stasińska G., Gomes J. M., 2005, MNRAS, 358, 363
Deo R., Crenshaw D., Kraemer S., Dietrich M., Elitzur M., Teplitz H., Turner T., 2007, ApJ, 671, 124
Desai V. et al., 2007, ApJ, 669, 810
Diamond-Stanic A. M., Rieke G., 2010, AAS Meeting Abstracts, #215

Dors O., Jr., Arellano-Córdova K., Cardaci M. V., Hägele G. F., 2017, MNRAS, 468, L113
Dors O., Jr., Cardaci M. V., Hägele G. F., Rodrigues I., Grebel E., Pilyugin L., Freitas-Lemes P., Krabbe A., 2015, MNRAS, 453, 4102
Dors O., Jr., Maiolino R., Cardaci M., Hägele G., Krabbe A., Pérez-Montero E., Armah M., 2020, MNRAS, 496, 3209
Dors O. L., Monteiro A. F., Cardaci M. V., Hägele G. F., Krabbe A. C., 2019, MNRAS, 486, 5853
Draine B. T., Li A., 2001, ApJ, 551, 807
Ehrenfreund P., Rasmussen S., Cleaves J., Chen L., 2006, Astrobiology, 6, 490
Feltre A., Charlot S., Gutkin J., 2016, MNRAS, 456, 3354
Ferland G. et al., 2017, Rev. Mex. Astron. Astrofis., 53, 385
Galliano F., Madden S. C., Tielens A. G., Peeters E., Jones A. P., 2008, ApJ, 679, 310
Hägele G. F., Díaz Á. I., Terlevich E., Terlevich R., Pérez-Montero E., Cardaci M. V., 2008, MNRAS, 383, 209
Hanine M., Meng Z., Lu S., Xie P., Picaud S., Devel M., Wang Z., 2020, ApJ, 900, 188
Hermandez-Jimenez, 2015, MNRAS, 451, 2278
Hernán-Caballero A., Hatziminaoglou E., 2011, MNRAS, 414, 500
Hernandez-Jimenez, 2013, MNRAS, 435, 3342
Houck J. R. et al., 2004, ApJS, 154, 18
Hudgins D. M., Bauschlicher C. W., Jr., Allamandola L., 2005, ApJ, 632, 316
Hummer D., Storey P., 1987, MNRAS, 224, 801
Jochims H., Ruhl E., Baumgartel H., Tobita S., Leach S., 1994, ApJ, 420, 307
Kammoun E. S. et al., 2019, ApJ, 877, 102
Kauffmann G. et al., 2003, MNRAS, 346, 1055 (Ka03)
Keel W., 1984, ApJ, 282, 75
Kennicutt R. C., Jr., Bresolin F., Garnett D. R., 2003, ApJ, 591, 801
Kewley L. J., Dopita M., Sutherland R., Heisler C., Trevena J., 2001, ApJ, 556, 121 (Ke01)
Kewley L. J., Nicholls D. C., Sutherland R. S., 2019, ARA&A, 57, 511
Li A., 2020, Nature Astron., 4, 339
Liu C. T., Kennicutt R. C., Jr., 1995, ApJ, 450, 547
Madden S. C., Galliano F., Jones A. P., Sauvage M., 2006, A&A, 446, 877
Maragkoudakis A., Ivkovich N., Peeters E., Stock D., Hemachandra D., Tielens A., 2018, MNRAS, 481, 5370
Martins-Franco Y., Menéndez-Delmestre K., 2021, Astron. Nach., 342, 186
Mateus A., Sodré L., Fernandes R. C., Stasińska G., Schoenell W., Gomes J. M., 2006, MNRAS, 370, 721
Mattioda A. et al., 2020, ApJS, 251, 22
McCarthy M. C., McGuire B. A., 2021, J. Phys. Chem., 125, 3231
McGuire B. A. et al., 2021, Science, 371, 1265
McGuire B. A., Burkhardt A. M., Kalenskii S., Shingledecker C. N., Remijan A. J., Herbst E., McCarthy M. C., 2018, Science, 359, 202
Miller B. P., Brandt W. N., Schneider D. P., Gibson R. R., Steffen A. T., Wu J., 2011, ApJ, 726, 20
Moustakas J., Kennicutt, Robert C. J., Tremonti C. A., Dale D. A., Smith J.-D. T., Calzetti D., 2010, ApJS, 190, 233
O'Dowd M. J. et al., 2009, ApJ, 705, 885
Peeters E., Bauschlicher C. W., Jr., Allamandola L. J., Tielens A. G., Ricca A., Wolfire M. G., 2017, ApJ, 836, 198
Peeters E., Hony S., Van Kerckhoven C., Tielens A., Allamandola L., Hudgins D., Bauschlicher C., 2002, A&A, 390, 1089
Peeters Z., Botta O., Charnley S., Kisiel Z., Kuan Y.-J., Ehrenfreund P., 2005, A&A, 433, 583
Prieto C. A., Lambert D. L., Asplund M., 2001, ApJ, 556, L63
Ricca A., Bauschlicher C. W., Roser J. E., Peeters E., 2018, ApJ, 854, 115
Ricca A., Roser J. E., Peeters E., Boersma C., 2019, ApJ, 882, 56
Ruschel-Dutra D., Pastoriza M., Riffel R., Sales D. A., Winge C., 2014, MNRAS, 438, 3434
Rush B., Malkan M. A., Spinoglio L., 1993, ApJS, 89, 1
Sales D. A., Pastoriza M. G., Riffel R., 2010, ApJ, 725, 605
Sales D. A., Pastoriza M. G., Riffel R., Winge C., 2013, MNRAS, 429, 2634
Schlemmer S., Giesen T., Mutschke H., 2014, Laboratory Astrochemistry: From Molecules through Nanoparticles to Grains, John Wiley & Sons, Weinheim, Germany
Schrum J. P., Zhu T. F., Szostak J. W., 2010, Cold Spr. Harbor Persp. Bio., 2, a002212
Seok J. Y., Hirashita H., Asano R. S., 2014, MNRAS, 439, 2186
Shannon M. J., Boersma C., 2019, ApJ, 871, 124
Shipley H. V., Papovich C., Rieke G. H., Brown M. J., Moustakas J., 2016, ApJ, 818, 60
Sidhu A., Peeters E., Cami J., Knight C., 2020, MNRAS, 500, 177
Smith J.-D. T. et al., 2007, ApJ, 656, 770
Sturm E., Thornley M., Lutz D., Kunze D., Moorwood A., Feuchtgruber H., Genzel R., Tran D., 2000, A&A, 358, 481
Tananbaum H. et al., 1979, ApJ, 234, L9
Tielens A. G., 2005, The Physics and Chemistry of the Interstellar Medium, Cambridge Univ. Press, Cambridge
Tielens A. G., 2008, ARA&A, 46, 289
Tielens A., 2013, Rev. Mod. Phys., 85, 1021
Véron-Cetty M. P., Véron P., 2003, A&A, 412, 399
Werner M. W. et al., 2004, ApJS, 154, 1
Wu Y., Charmandaris V., Huang J., Spinoglio L., Tommasin S., 2009, ApJ, 701, 658
Xie Y., Li A., Hao L., 2017, ApJS, 228, 6
Yang X. J., Glaser R., Li A., Zhong J. X., 2017, New A Rev., 77, 1
Zhu S. F., Brandt W. N., Wu J., Garmire G. P., Miller B. P., 2019, MNRAS, 482, 2016

SUPPORTING INFORMATION

Supplementary data are available at *MNRAS* online.

Table C1. Species of PAHs that are contributing to the total emission in IR spectrum of Mrk 273.
Table C2. Same as Table C1, but for Mrk 471.
Table C3. Same as Table C1, but for Mrk 609.
Table C4. Same as Table C1, but for Mrk 622.
Table C5. Same as Table C1, but for Mrk 883.
Table C6. Same as Table C1, but for NGC 660.
Table C7. Same as Table C1, but for NGC 2622.
Table C8. Same as Table C1, but for NGC 2623.
Table C9. Same as Table C1, but for NGC 4676.
Table C10. Same as Table C1, but for NGC 4922.
Table C11. Same as Table C1, but for NGC 5256.
Table C12. Same as Table C1, but NGC 5347.

Please note: Oxford University Press is not responsible for the content or functionality of any supporting materials supplied by the authors. Any queries (other than missing material) should be directed to the corresponding author for the article.

APPENDIX A: PAHFIT SPECTRA DECOMPOSITION

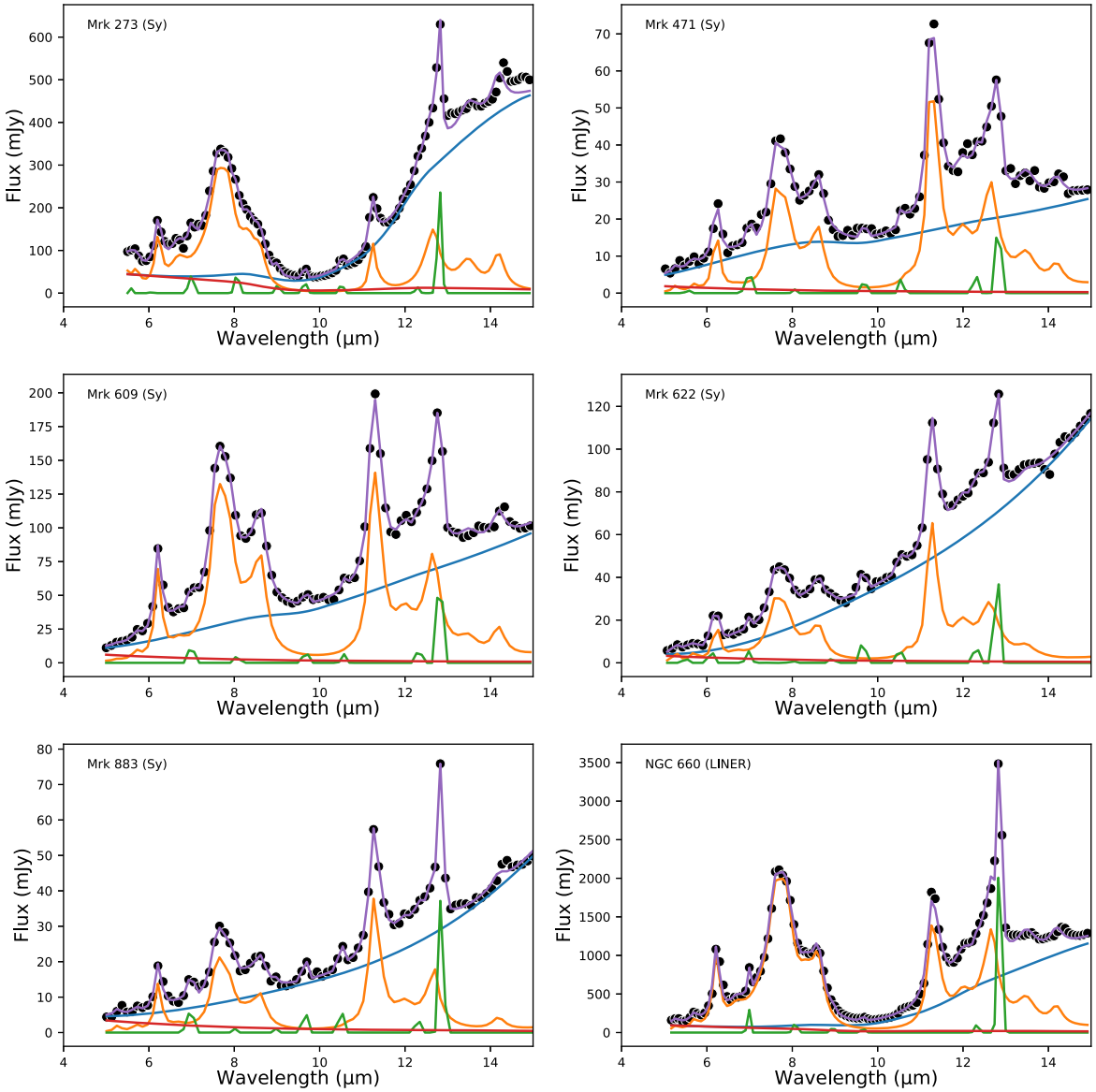

Figure A1. PAHFIT decomposition of our galaxies from 5 to 15 μm in components of the total continuum (blue line), stellar continuum (red line), ionic lines (green line), PAH and dust features (orange line) and the best-fitting model (purple line). The data points are shown in black.

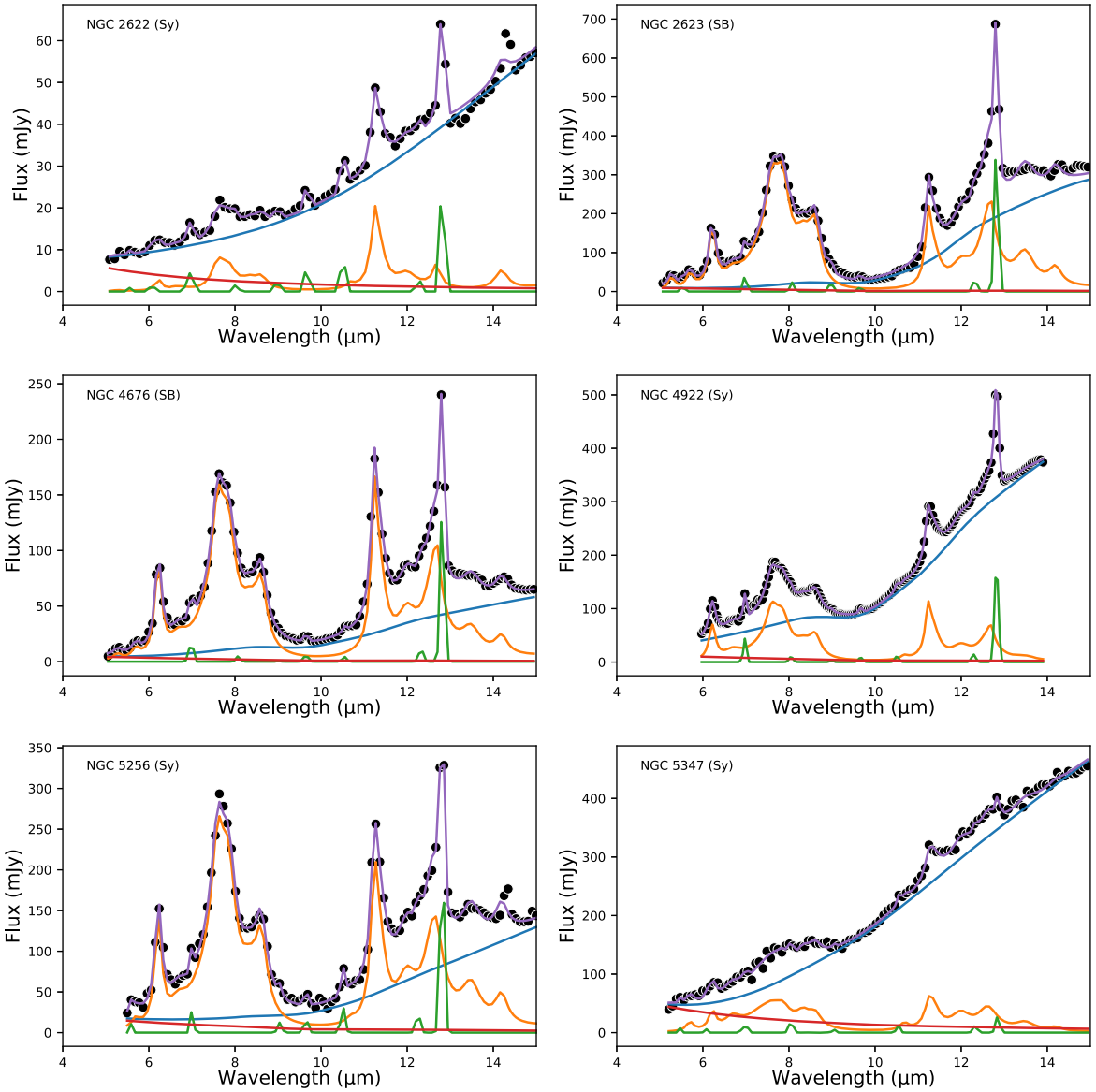

Figure A2. PAHFIT decomposition of our galaxies from 5 to 15 μm in components of the total continuum (blue line), stellar continuum (red line), ionic lines (green line), PAH and dust features (orange line) and the best-fitting model (purple line). The data points are shown in black.

APPENDIX B: PAHDB FITTING

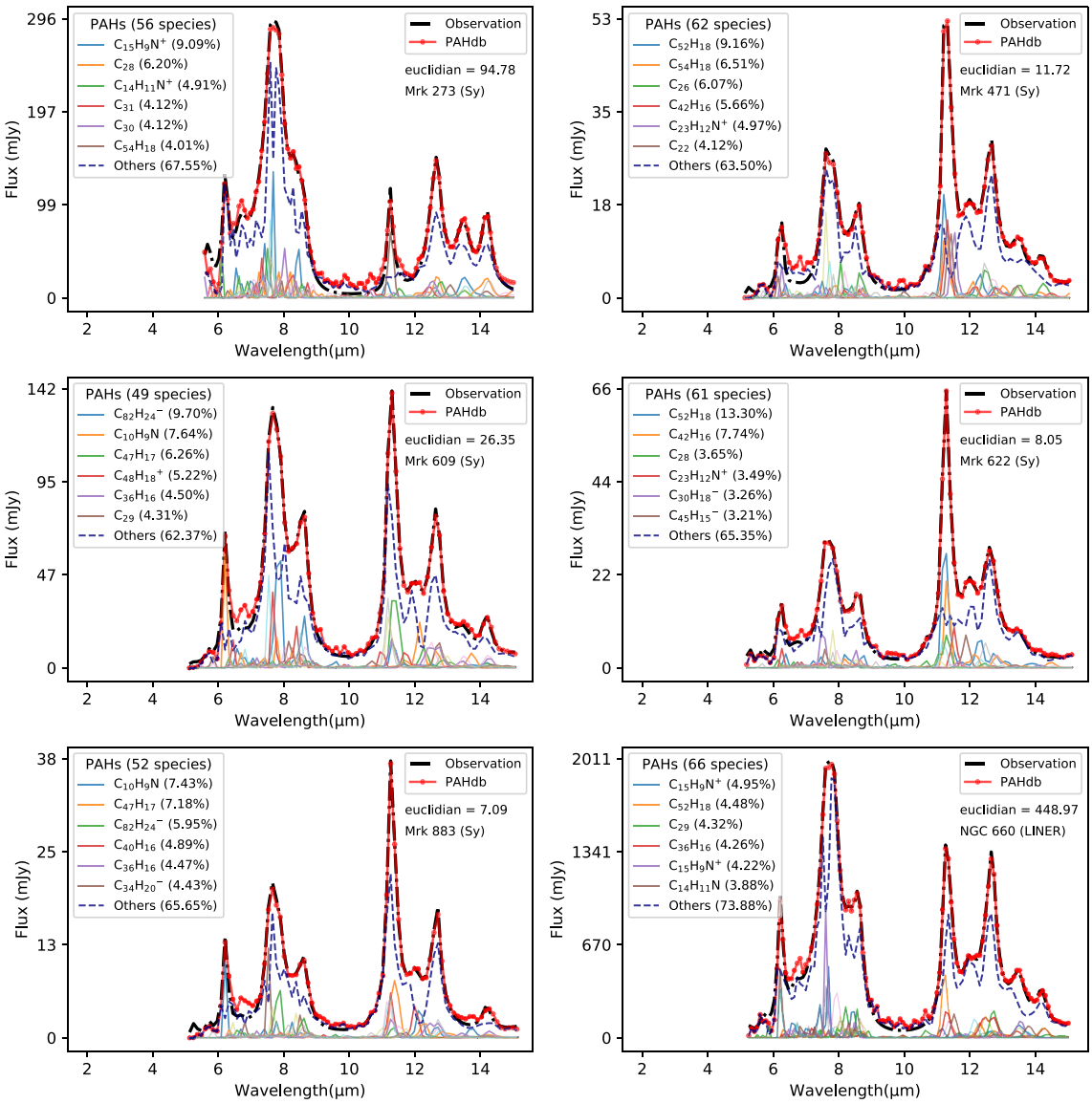

Figure B1. The PAHdb fit to the observed spectrum for the remaining of the objetcs of our sample. The quality of the fitting is quantified by the parameter Euclidean. The fractional contribution to the flux from the species is shown.

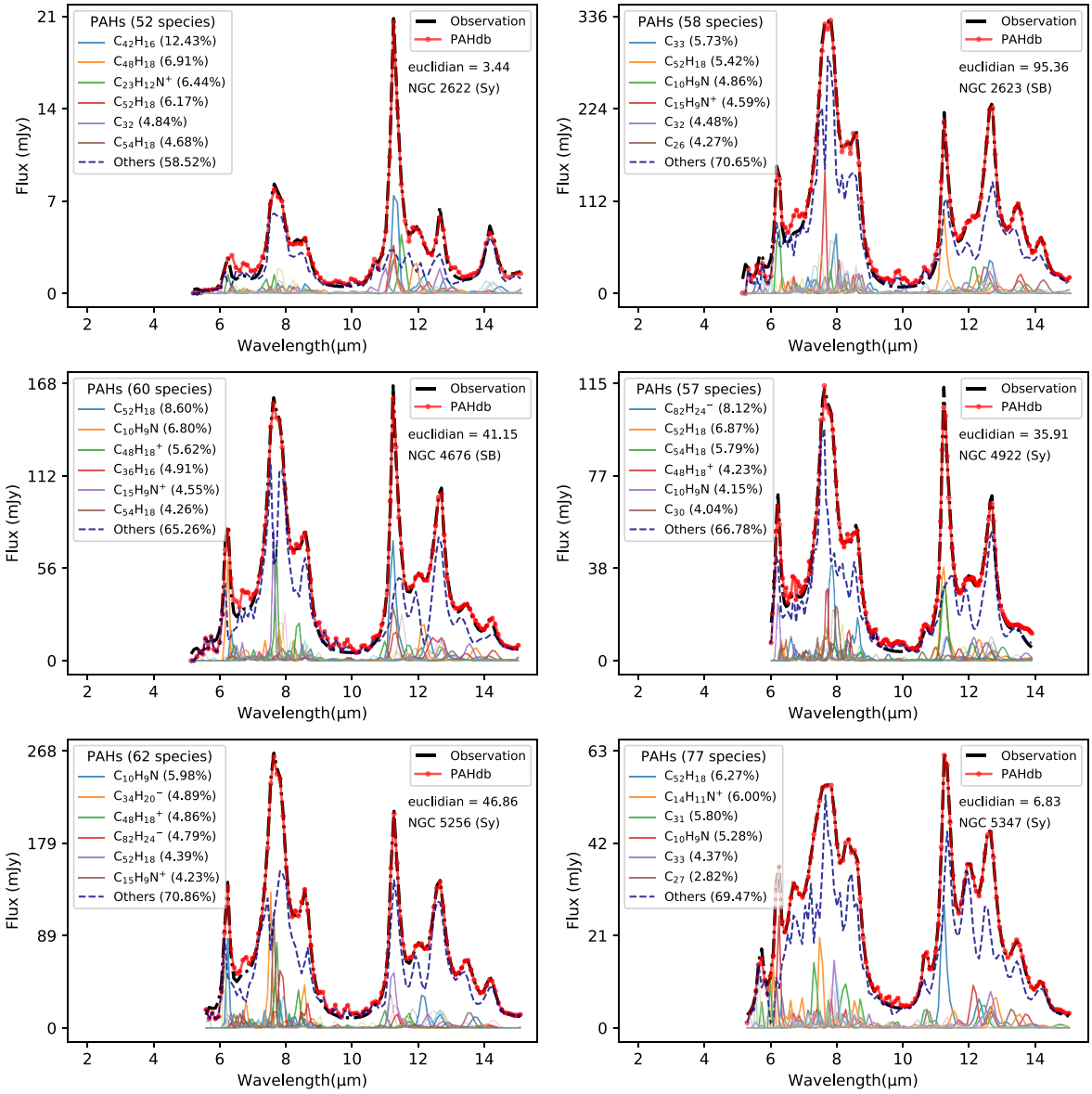

Figure B2. The PAHdb fit to the observed spectrum for the remaining of the objetcs of our sample. The quality of the fitting is quantified by the parameter Euclidean. The fractional contribution to the flux from the species is shown.

APPENDIX C: SPECIES EMISSIONS EACH GALAXY

Table C1. Species of PAHs that are contributing to the total emission in IR spectrum of Mrk 273. The full table is available online.

UID	Formula	Charge	Per cent
470	$C_{15}H_9N^+$	1	9.1
2482	C_{28}	0	6.2
480	$C_{14}H_{11}N^+$	1	4.9
2758	C_{31}	0	4.1
2598	C_{30}	0	4.1
⋮	⋮	⋮	⋮

Table C2. Same as Table C1 but for Mrk 471. The full table is available online.

UID	Formula	Charge	Per cent
3173	$C_{52}H_{18}$	0	9.0
836	$C_{54}H_{18}$	0	6.7
2427	C_{26}	0	6.1
620	$C_{42}H_{16}$	0	5.7
233	$C_{23}H_{12}N^+$	1	5.0
⋮	⋮	⋮	⋮

Table C3. Same as Table C1 but for Mrk 609. The full table is available online.

UID	Formula	Charge	Per cent
3205	$C_{82}H_{24}^{-}$	−1	9.7
473	$C_{10}H_9N$	0	7.7
76	$C_{47}H_{17}$	0	6.2
636	$C_{48}H_{18}^{+}$	1	5.3
128	$C_{36}H_{16}$	0	4.5
⋮	⋮	⋮	⋮

Table C4. Same as Table C1 but for Mrk 622. The full table is available online.

UID	Formula	Charge	Per cent
3173	$C_{52}H_{18}$	0	13.3
620	$C_{42}H_{16}$	0	7.8
2494	C_{28}	0	3.6
233	$C_{23}H_{12}N^{+}$	1	3.5
724	$C_{45}H_{15}^{-}$	−1	3.3
⋮	⋮	⋮	⋮

Table C5. Same as Table C1 but for Mrk 883. The full table is available online.

UID	Formula	Charge	Per cent
76	$C_{47}H_{17}$	0	7.5
473	$C_{10}H_9N$	0	7.4
3205	$C_{82}H_{24}^{-}$	−1	6.0
625	$C_{40}H_{16}$	0	4.9
128	$C_{36}H_{16}$	0	4.5
⋮	⋮	⋮	⋮

Table C6. Same as Table C1 but for NGC 660. The full table is available online.

UID	Formula	Charge	Per cent
470	$C_{15}H_9N^{+}$	1	5.0
3173	$C_{52}H_{18}$	0	4.5
2542	C_{29}	0	4.3
128	$C_{36}H_{16}$	0	4.3
468	$C_{15}H_9N^{+}$	1	4.2
⋮	⋮	⋮	⋮

Table C7. Same as Table C1 but for NGC 2622. The full table is available online.

UID	Formula	Charge	Per cent
620	$C_{42}H_{16}$	0	13.3
635	$C_{48}H_{18}$	0	6.8
233	$C_{23}H_{12}N^{+}$	1	6.8
3173	$C_{52}H_{18}$	0	6.4
2782	C_{32}	0	4.7
⋮	⋮	⋮	⋮

Table C8. Same as Table C1 but for NGC 2623. The full table is available online.

UID	Formula	Charge	Per cent
2955	C_{33}	0	5.7
3173	$C_{52}H_{18}$	0	5.4
473	$C_{10}H_9N$	0	4.9
468	$C_{15}H_9N^{+}$	1	4.6
2791	C_{32}	0	4.5
⋮	⋮	⋮	⋮

Table C9. Same as Table C1 but for NGC 4676. The full table is available online.

UID	Formula	Charge	Per cent
3173	$C_{52}H_{18}$	0	8.6
473	$C_{10}H_9N$	0	6.8
636	$C_{48}H_{18}^{+}$	1	5.6
128	$C_{36}H_{16}$	0	4.9
468	$C_{15}H_9N^{+}$	1	4.5
⋮	⋮	⋮	⋮

Table C10. Same as Table C1 but for NGC 4922. The full table is available online.

UID	Formula	Charge	Per cent
3205	$C_{82}H_{24}^{-}$	−1	8.1
3173	$C_{52}H_{18}$	0	6.9
836	$C_{54}H_{18}$	0	5.8
636	$C_{48}H_{18}^{+}$	1	4.2
473	$C_{10}H_9N$	0	4.1
⋮	⋮	⋮	⋮

Table C11. Same as Table C1 but for NGC 5256. The full table is available online.

UID	Formula	Charge	Per cent
473	$C_{10}H_9N$	0	6.0
822	$C_{34}H_{20}^{-}$	−1	4.9
636	$C_{48}H_{18}^{+}$	1	4.9
3205	$C_{82}H_{24}^{-}$	−1	4.8
3173	$C_{52}H_{18}$	0	4.4
⋮	⋮	⋮	⋮

Table C12. Same as Table C1 but NGC 5347. The full table is available online.

UID	Formula	Charge	Per cent
3173	$C_{52}H_{18}$	0	6.3
480	$C_{14}H_{11}N^{+}$	1	6.0
2758	C_{31}	0	5.8
473	$C_{10}H_9N$	0	5.4
2955	C_{33}	0	4.3
⋮	⋮	⋮	⋮

APPENDIX D: PEETERS' CLASSIFICATION PROCEDURE

The PAH band profile variations were studied in several astrophysical objects by Peeters et al. (2002), which separated those bands intro three different classes (A, B, and C), according to their central wavelengths. The 6–9 μm spectral region, in special, is composed by three PAH main features: a band at 6.2 μm, a complex of overlapping bands at 7.7 μm with two components at 7.6 and 7.8 μm, and a band at 8.6 μm (Ricca et al. 2018). In the case of the first band, the profile A peaks at shorter wavelengths in comparison to B and C profiles. For the 7.7-μm complex, the Classes A and B differ in the relative strength of the 7.6 and 7.8 μm features ($F_{7.6}/F_{7.8}$ flux ratio), which seem to be shifted to a peak position of 8.2 μm for Class C objects (Tielens 2008). Finally, the 8.6 μm band also peaks at shorter wavelengths for A profiles.

The methodology applied to classify the NGC 2622, NGC 4922, and NGC 5347 galaxies is the same used in the other objects of our sample, previously performed by Canelo et al. (2018, 2020, 2021). The PAHFIT decomposition does not allow the band central wavelengths to vary and can not be used to this analysis. Therefore, we subtracted the underlying continuum with a spline decomposition (e.g. Galliano et al. 2008; Peeters et al. 2017), with a set of anchor points at roughly 5.4, 5.8, 6.6, 7.2, 8.2, 9.0, 9.3, 9.9, 10.2, 10.9, 11.7, 12.1, 13.1, 13.9, 14.7, and 15.0 μm. In sequence, the 6.2, 7.7, and 8.6 μm bands were independently fitted with a Gaussian profile (based on the procedure of Peeters et al. 2017, for instance), with a PYTHON-based script constructed to estimate their central wavelength (λ_c), amplitude and FWHM through the optimization algorithms from the submodule *scipy.optmize.curve_fit*. The uncertainties of these parameters were also derived by this tool with least-squares minimization from the flux uncertainties provided by the ATLAS. The initial guesses for the parameters were selected from Smith et al. (2007). The continuum and bands fitting are shown in Fig. D1 and Table D1. In the specific case of the 7.7 μm complex, we fixed the FWHM values according to Peeters et al. (2002) in 0.28–7.6 and 0.32–7.8 μm profiles, respectively, to avoid the blending of the features.

The particular case of NGC 5347 needed a slightly different approach. The PAH emissions are weaker in this galaxy and the 7–10 μm region resembles a unique bump feature, as expected in Class C objects. As a matter of fact, this source was already pointed out as Compton-thick AGN, with a dusty material obscuring the central engine (Kammoun et al. 2019). In order to proper analyse NGC 5347, the anchor point at 8 μm was not included in the spline decomposition and the 7.7- and 8.6-μm bands were fitted with just one broad Gaussian profile with peak position at roughly 8.22 μm (see for example Peeters et al. 2002). In such objects, the

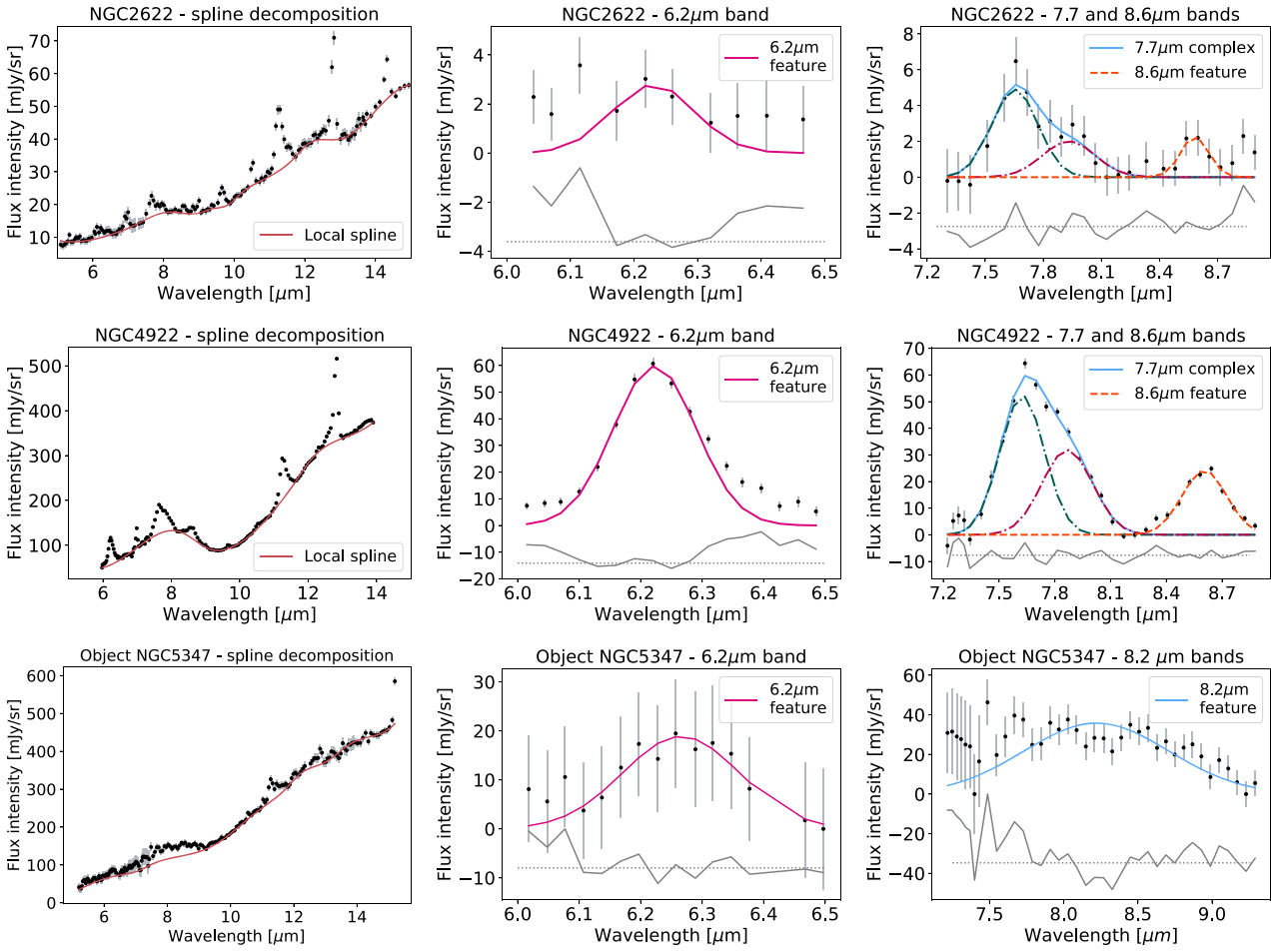

Figure D1. Local spline decomposition and fit results of the 6.2, 7.7, and 8.6 bands for the galaxies of NGC 2622, NGC 4922, and NGC 5347, from top to down. The data points and error bars are in black and grey, respectively.

Table D1. The best-fitting results for the 6.2-, 7.7-, and 8.6-μm bands. A is the amplitude in mJy sr^{-1}, λ_c is the central wavelength in μm and FWHM is the full width at half-maximum.

Source	λ_c	Err	A	Err	FWHM	Err
NGC 2622	6.231	0.011	0.455	0.078	0.153	0.032
	7.653	0.024	1.460	0.171	0.280	–
	7.932	0.051	0.684	0.166	0.320	–
	8.582	0.014	0.413	0.069	0.170	0.033
NGC 4922	6.223	0.002	10.130	0.248	0.159	0.005
	7.625	0.009	15.574	0.845	0.280	–
	7.867	0.014	10.859	0.844	0.320	–
	8.604	0.005	7.271	0.312	0.283	0.015
NGC 5347	6.266	0.007	4.488	0.290	0.223	0.018
	8.221	0.048	43.786	3.868	1.150	0.122

7.7 μm corresponds to a Class C object and there is no emission at 8.6 μm.

With the results of the Gaussian fits, it is possible to separate the sources into the Peeters' classes. The 6.2-μm band is considered as Class A if $\lambda_c < 6.23$ μm, Class B if $6.23 < \lambda < 6.29$ μm, and Class C if $\lambda_c > 6.29$. The 7.7-μm complex is considered as Class A if $F_{7.6}/F_{7.8} \geq 1$, Class B if $F_{7.6}/F_{7.8} < 1$, and Class C if $\lambda_c \sim 8.22$ μm (the 7.6 and 7.8 μm features are not present). The 8.6-μm band does not have a Class C profile, and the A and B classifications depend on whether $\lambda_c < 8.60$ μm or $\lambda_c > 8.60$ μm, respectively. The classification of NGC 2622, NGC 4922, and NGC 5347 are displayed in Table 6. The $F_{7.6}/F_{7.8}$ ratios of NGC 2622 and NGC 4922 are 2.187 ± 0.513 and 1.444 ± 0.134, respectively.

This paper has been typeset from a TEX/LATEX file prepared by the author.